Design, Modeling and Characterization of a Multiscale Heat Exchanger for High-Temperature, High-Pressure Applications

by

Chad T. Wilson

B.S.E. Mechanical Engineering
University of Michigan, 2019

Submitted to the Department of Mechanical Engineering
in partial fulfillment of the requirements for the
Degree of Master of Science in Mechanical Engineering
at the
MASSACHUSETTS INSTITUTE OF TECHNOLOGY
June 2021

Author ....

Department of Mechanical Engineering

May 14, 2021

Certified by ....

Evelyn N. Wang

Department Head, Gail E. Kendall Professor of Mechanical Engineering

Thesis Supervisor

Accepted by ....

Nicolas Hadjiconstantinou

Chairman, Department Committee on Graduate Theses

Design, Modeling and Characterization of a Multiscale Heat Exchanger for High-Temperature, High-Pressure Applications

by

Chad Wilson

Abstract

Heat exchangers are devices that facilitate thermal energy transfer between two or more mediums and which function as key components in many industrial processes, such as steam power plants, refrigeration, chemical plants, nuclear plants, refineries, and next-generation renewable energy storage processes. Recent advancements in power generation techniques and heat engine cycle structures offer potential improvements to the efficiency of each process but require components capable of operating in increasingly demanding environments. Specifically, the shift to high-temperature, high-pressure thermodynamic cycles for improved efficiency has offered a new opportunity for device-level innovations, including producing a heat exchanger that supersedes classical material and design operating limits. Previous work has attempted to infiltrate this new market by developing heat exchangers using costly metal materials in mature architectures that achieve low power densities. Silicon carbide, while well known as a high-temperature material, has rarely been used under such loading conditions due to its low resistance to fracture and high tensile stress concentrations featured in existing heat exchanger designs.

In this thesis, we present the design, structural modelling, and initial characterization of a multiscale ceramic heat exchanger, capable of operating in extreme environments with high power densities and a safety factor against mechanical failure. The heat exchanger device is evaluated for a supercritical CO_2 Brayton cycle, using air and sCO_2 as working fluids at 80 bar, 1300 °C and 250 bar, 300 °C, respectively. A multiscale channel design, enabled by ceramic co-extrusion, results in a counterflow heat exchanger core with both high thermal performance and high mechanical strength during steady state operation. For

coupling this core to typical power-cycle tubing we designed manufacturable ceramic headers, whose geometry was optimized to minimize both pressure loss and flow maldistribution of the working fluids. To evaluate prototypes of our design, we constructed a test setup and experimentally quantified the performance of initial heat exchanger core components. Our design offers a practical solution to address the material limitations imposed by high-temperature, high-pressure thermodynamic cycles while predicting efficiency and performance improvements compared to current state-of-the-art heat exchanger alternatives.

Thesis Supervisor: Evelyn N. Wang
Title: Department Head; Gail E. Kendall Professor

Acknowledgments

First and foremost I would like to thank my advisor, Evelyn N. Wang, whose guidance and support is instrumental to the ongoing success of this project. Thank you also to ARPA-E for funding this work and providing consistent, valuable feedback as to the direction of this project.

Thank you to my collaborators Rodney W. Trice, Jeffrey P. Youngblood, Olivia N. Brandt and Rodrigo Orta Guerra at Purdue University and Gregory Natsui and the rest of the team at General Electric (GE) for their contributions to this work.

Xiangyu Li has been an essential colleague, mentor, and resource throughout my time as a graduate student at MIT, guiding me at the start of my work and providing much-needed intuition and feedback as the project progressed. His attention to detail on this project encourages me to think more critically about the underlying problem, and I have learned a great deal from our heat transfer talks. I admire his aptitude as a researcher and look forward to our future work together.

Thank you to all the members of the Device Research Lab for their continued support and welcoming attitudes, I feel at home here at MIT in part because of you all. I thank Arny Leroy and the rest of the solar subgroup for always inciting helpful discussions and sharing phenomenal ideas, along with ample constructive criticism, to dramatically improve my work.

I am lucky to have met Cody Jacobucci and Carlos Diaz, two fellow DRL members, whose academic support, friendship, and company at the gym kept me motivated through the unprecedented covid-19 era. Thank you to all my amazing friends who have supported me during my time at MIT, fresh air was often my way of recharging and I value our climbing, hiking, and snowboarding adventures above all.

Lastly, thank you to my family for their unwavering support of all that I do. I will always be competing with my brother Matt, whether he knows it or not, and it is because of him that I am who I am today. My sister Abby always knows how to cheer me up, and the thought of her drives me through difficult times. I admire both of you and could not have asked for better siblings. To my parents, thank you for teaching me the value of knowledge and curiosity, and for supporting me unequivocally. I am so thankful to have you all on my team.

Table of Contents

List of Figures

12

Chapter 1

1. Introduction

1.1. MOTIVATION

The U.S. Energy Information Administration (EIA) [1] estimated that 60% of the energy consumed for electricity generation was lost to the environment in 2019. Increasing the efficiency of power generation is one solution to address the dichotomy between globally increasing energy demand and limited fossil fuel resources [2]. Efficiency gains directly correlate to a reduction in the amount of fuel required per unit of energy produced, which has the potential to reduce harmful by-product emissions such as carbon dioxide, a major contributor to global climate change [3]. State-of-the-art power generation and storage systems, based on renewable energy sources, will also benefit from more efficient thermodynamic cycle components.
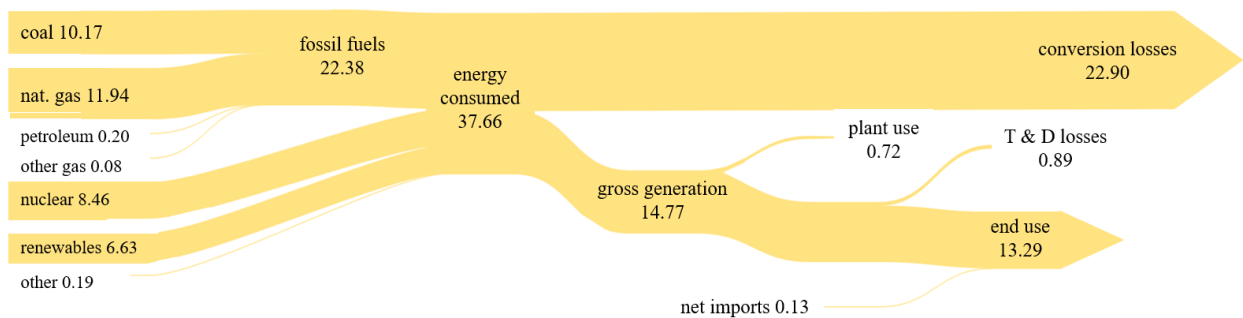
Figure 1 – United States 2019 electricity production flow in quadrillion BTU [1]**.**

Thus, there exists an opportunity to develop more efficient power generation and recovery systems that allow for significant energy savings and an overall reduction in fuel consumption. Heat engines have undergone centuries of innovation to improve their efficiency, for applications ranging from electricity generation to transportation, energy storage to waste heat recovery. Independent of initial fuel source or process, a universally efficient heat exchanger subsystem can be implemented both in existing fossil fuel power generation heat engines and in emerging renewable resource and transportation solutions to improve the efficiency of thermal energy exchange in a thermodynamic cycle. Recently, to both lower the levelized cost of electricity in terrestrial power generation plants [4] and reduce the mass requirement for onboard electricity generation in aviation [5], academic research has focused on increasing the operating temperatures and pressures of these thermodynamic power cycles [6][7]. While progress has been made on developing the working fluids required for such cycles, like supercritical CO_2 (sCO_2) and molten salts, the

heat exchanger subcomponent remains a key limiting factor in the implementation of these high-temperature, high- pressure thermodynamic power cycles [8].

Heat exchangers are an integral part of many power generation cycles, responsible for the thermal exchange of energy between two or more working fluids. While not application specific, the following heat exchanger design proposed in this thesis focuses primarily on a sCO_2 Brayton cycle [9], intended for an aircraft's auxiliary power unit (APU) as a waste-recovery and thermal management system [5]. Typical gas turbine APUs consume about 2% of a vehicles total fuel consumption [10], amounting to roughly 50 kg per hour of flight time for a medium commercial plane like the Boeing 737-200 [11]. Weight is an enormous limitation to the aviation industry; therefore, even a relatively small improvement in APU efficiency can reduce the fuel storage by kilos and save money on fuel, as well as reduce the overall emissions of an airplane in-flight. An efficiency improvement goal drives companies like General Electric to pursue new APU system configurations, such as a sCO_2 Brayton cycle, that has a marked improvement over other power cycle architectures [12].

1.2. BACKGROUND

Heat exchangers capable of withstanding extreme temperatures have recently been in high demand. Several solutions using classic heat exchanger architectures are listed in Table 1, most of which rely on expensive nickel-based superalloys to survive the high temperature conditions. These heat exchanger solutions also typically consist of geometries ill-suited for achieving high mass- and volume-based energy densities. Figure 2 shows common heat exchanger materials with respect to operating temperatures and material strength, highlighting recent focus on silicon carbide (SiC) and similar ceramics rather than superalloys due to higher melting points and higher material strengths at elevated temperatures. Structural integrity of the superalloy solutions suffers at increased operating temperatures – a dependency not seen with ceramic solutions.
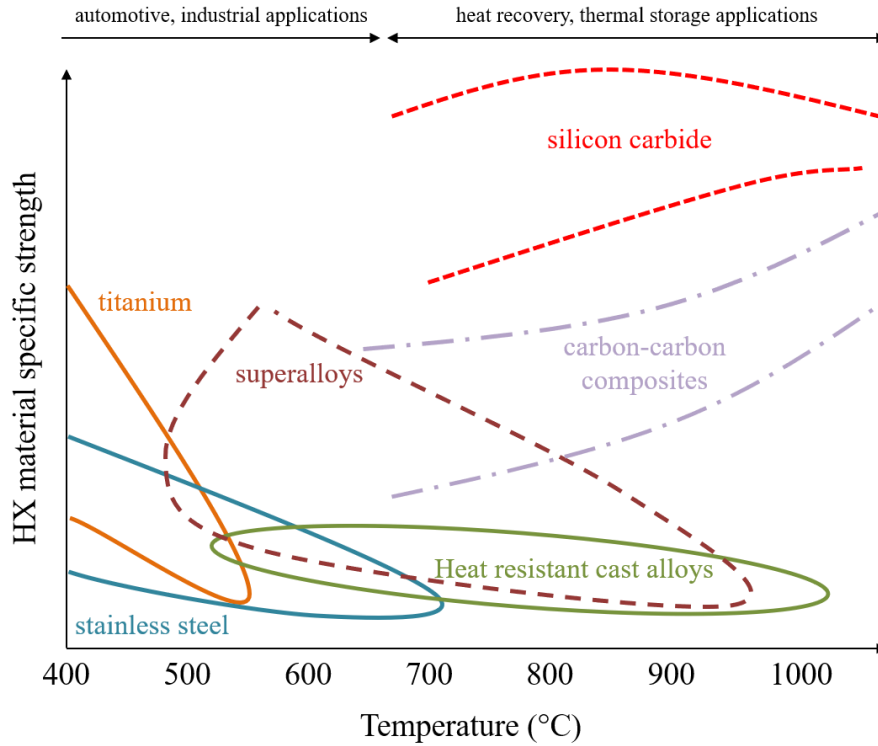
Figure 2 – Operating temperature ranges and corresponding specific strength for various heat exchanger materials (adapted from [13])**.**

Table 1 – State-of-the-art heat exchanger comparison

Type	A_{ht}/V (m²/m³)	T_{max} (°C)	P_{max} (bar)	Material (for T_{max} use)	Reference
Shell-and-tube heat exchanger	50 - 100	1100	1000	expensive metal alloys	[14]
Plate-and-frame heat exchanger	120 - 660	815	200	expensive metal alloys	[14]
Plate-fin heat exchanger	800 - 1500	800	120	stainless steel	[15]
Printed circuit heat exchanger (PHE)	500 - 800	> 750	200	Ceramic-metal composite (ZrC + W)	[16]

Current on-the-market ceramics listed in Table 2 offer points of comparison when discussing the strength of a ceramic heat exchanger and will frequently be referred to in the structural evaluation stage of this report. However, it should be noted that the ultimate tensile strength of silicon carbide varies widely in industry, and depends on manufacturing parameters such as sintering temperature, pressure, time, and type of synthesis.

Table 2 – Current on-the-market high-temperature material properties and limitations

Material	Tensile Strength (MPa)	Notes
SUPERSIC-1 [17]	159 ± 14	100% β-SiC, 20% porosity. Powder-sintered. No effect of temperature on strength up to 1500 °C.
SUPERSIC-2 [17]	186 ± 23	SUPERSIC-1 + CVD SiC coating. Comparatively much less porous. No effect of temperature on strength up to 1500 °C.
Morgan Advanced Materials [18]	370 (20 °C) – 560 (1300 °C)	SiC manufactured via CVD, stated as "dense" with 99.9995% purity.
Inconel 625 Alloy [19]	830 (20 °C) – 138 (980 °C)	Ni-based superalloy. Max operating temperature 1000 °C. Strength strongly dependent on operating temperature
Rene 41 [20]	1420 (21 °C) – 400 (927 °C)	Precipitation hardening, nickel-based high temperature alloy. Max operating temperature 1000 °C. Strength strongly dependent on operating temperature

1.3. THESIS OBJECTIVES AND OUTLINE

The objective of this thesis is to present the modelling and design of a heat exchanger capable of performing in high-temperature and high-pressure environments without mechanically failing, and to illustrate how this design can be tested in a laboratory setting. The design relies on a ceramic co-extrusion technique to fabricate a multi-scale heat exchanger core, geometrically optimized to achieve designated thermal performance metrics and a safety factor against failure. We developed multi-physics models of a potential header design to interface with this core, and evaluated its structural, fluidic, and thermal behavior. We fabricated an experimental setup to evaluate the performance of the heat exchanger core and headers and

16

demonstrated the effectiveness of this setup by quantifying the pressure loss of a heat exchanger core unit cell. The structure of this thesis is outlined below:

In Chapter 1, the motivation for designing a high-temperature, high-pressure heat exchanger is discussed. Previous designs and incentives for development are highlighted.

In Chapter 2, a framework for heat exchanger evaluation and details of our patented solution to a high-temperature, high-pressure ceramic heat exchanger are reviewed.

In Chapter 3, structural analysis of the heat exchanger core is presented, including results based on the target geometry and results adjusted for potential manufacturing defects, variations. Structural failure of the heat exchanger core is also discussed.

In Chapter 4, the design and optimization of heat exchanger headers is presented, with a focus on pressure loss and flow maldistribution mitigation.

In Chapter 5, we discuss the fabrication of an experimental setup for testing heat exchanger components and show initial sample testing of a single unit cell. Values for thermal conductivity of our silicon carbide material are also experimentally obtained here.

In Chapter 6, future work necessary for this project to culminate into a functioning heat exchanger is explained.

Chapter 2

2. Heat exchangers

2.1. ARCHITECTURES

Heat exchangers are instrumental in many heat transfer applications, and as such come in a variety of designs. According to Shah *et al.*, whose work was instrumental in developing an intuition for heat exchanger designs and evaluations, heat exchangers are classified according to transfer processes, number of fluids, degree of surface compactness, construction features, flow arrangements, and heat transfer mechanisms [21]. Several heat exchanger architectures are commonplace in industry, including shell-and-tube, plate, plate-and-frame, and plate-fin heat exchangers. Two common flow arrangements, parallel flow and counterflow, are shown in Figure 3. While designs substantially differ based on application, some fundamental mechanisms of heat transfer and performance evaluation remain consistent across the spectrum.
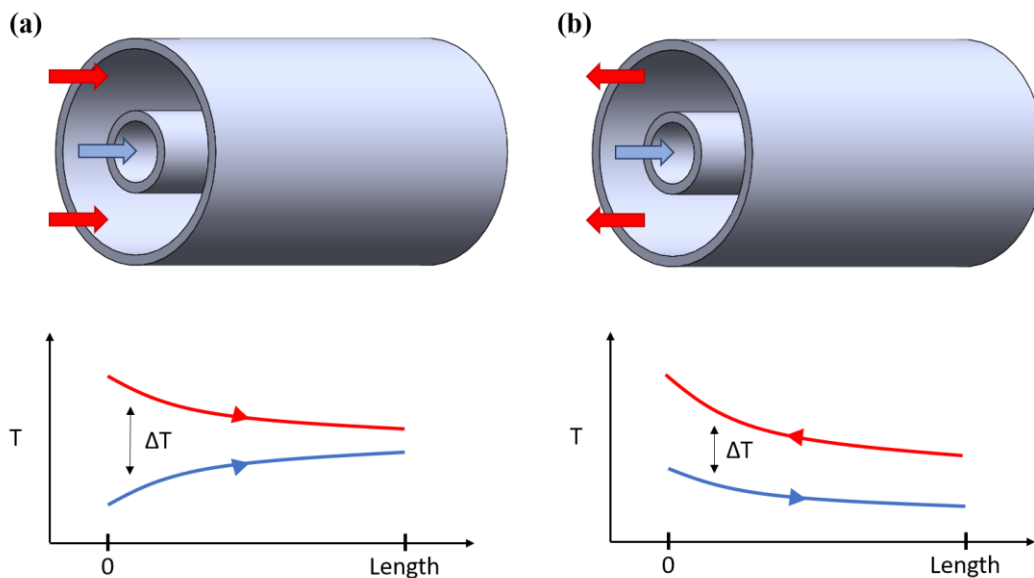
Figure 3 – Parallel (a) and counter-flow (b) shell-and-tube heat exchanger architectures, with corresponding temperature profiles, adapted from [22]**.**

Parallel flow architectures are constrained by an equivalent outlet temperature limit for both streams, which results in a diminishing temperature difference along the heat exchanger length. However, counterflow heat exchanger architectures allow for a nearly uniform temperature difference throughout the length of the

device, yielding a higher overall heat flux and thus performance compared to parallel flow systems. Because of this our proposed design features counterflowing working fluids.

2.2. MECHANICS OF HEAT TRANSFER IN HEAT EXCHANGERS

2.2.1. Theory of heat transfer

Overall, the goal of a heat exchanger is to facilitate transfer of thermal energy between two or more working fluids. Typically, no external heat or work interactions occur within a heat exchanger. Therefore, performance of a heat exchanger is quantified by determining how well thermal energy was transferred between mediums.

2.2.2. Key parameters, metrics for performance evaluation

Effectiveness is a measure of the thermal performance of the heat exchanger, defined by

$$\varepsilon = \frac{q}{q_{max}} \tag{1}$$

$$q_{max} = C_{min}\Delta T_{max} \tag{2}$$

where q is the actual rate of heat transfer from the hot fluid to the cold fluid and q_{max} is the maximum possible heat transfer rate thermodynamically permitted. C_{min} is the minimum heat capacitance, equal to the lesser of C_{hot} and C_{cold}. When designing a heat exchanger, it is typical to have a target effectiveness with which you then optimize the design to achieve high mass- and volume-based energy densities. For our target aviation application, the heat exchanger core is designed to achieve an effectiveness of 50% [23].

2.2.3. Necessity and challenges of high-temperature, high-pressure working fluids

Heat transfer systems may aim to increase overall operating temperatures and pressures to achieve higher overall efficiencies. This relationship is best shown when considering an ideal Carnot cycle, whose efficiency η_{max}, given by equation (3), is directly proportional to the ratio of cold side T_c to hot side T_h temperatures. In this way, increasing the hot side temperature results in an increase in efficiency.

$$\eta_{max} = 1 - \frac{T_c}{T_h} \tag{3}$$

Furthermore, a Brayton cycle efficiency, representing the operation of a gas turbine engine, can be calculated using equation (4),

19

$$\eta_B = 1 - \frac{1}{\left(\frac{P_d}{P_0}\right)^{\frac{\gamma-1}{\gamma}}}$$

(4)

where P_d is the compressor discharge pressure, P_o is the intake pressure, and γ is the heat capacity ratio. By increasing the pressure to the turbine, which in turn increases the pressure in the heat exchanger, cycle efficiency can be improved.

Additionally, high temperatures and pressures provide benefits for thermal energy storage applications, as they decrease the levelized cost of electricity by reducing the percentage of usable energy lost to the environment. Moreover, solar receivers in concentrated solar power plants require a heat exchanger capable of handling high temperature working fluids [15], as do various nuclear plants [24] and other energy sector cycles.

2.3. PROPOSED HEAT EXCHANGER DESIGN

This thesis focuses on a heat exchanger proposed as an ARPA-E funded project under HITEMMPS [25]. The project targets a 50 kW$_{th}$ heat exchanger capable of 50% effectiveness in a sCO$_2$ Brayton cycle, consisting of inlet air at 1285 °C, 8 MPa, 0.08 kg/s and inlet sCO$_2$ at 300 °C, 25 MPa, 0.08 kg/s. The volume-based and mass-based power densities are aimed to maximize weight and size constraints for aviation applications. The original design and its metrics serve as base lines for further optimization and evaluation work. Air and sCO$_2$ are the cold and hot working fluid respectively, moving counterflow through alternating macrochannels configured in a checkerboard pattern (Figure 4). This checkerboard grid is assembled using ceramic co-extrusion methods [26], where a square channel is forced through a 5:1 reducing die, stacked together into a 5x5 grid, and then extruded again. This process can continue to achieve increasingly smaller microchannel sizes. "Microchannel" refers to the individual channel through which a working fluid passes, which for this design is on the order of 200 μm wide. "Macrochannel" refers to the collection of microchannels that is formed following several co-extrusion steps and is associated with a specific working fluid. As proposed, this heat exchanger core consists of 18 hot and 18 cold macrochannels, each of which contains 625 microchannels. Currently, the design targets an effectiveness of 50% with a total pressure drop of < 4% for each fluid and a safety factor against mechanical failure. Structural analysis is the focus of this report, as failure of the core is directly coupled with its ability to withstand the high-pressure operating conditions.
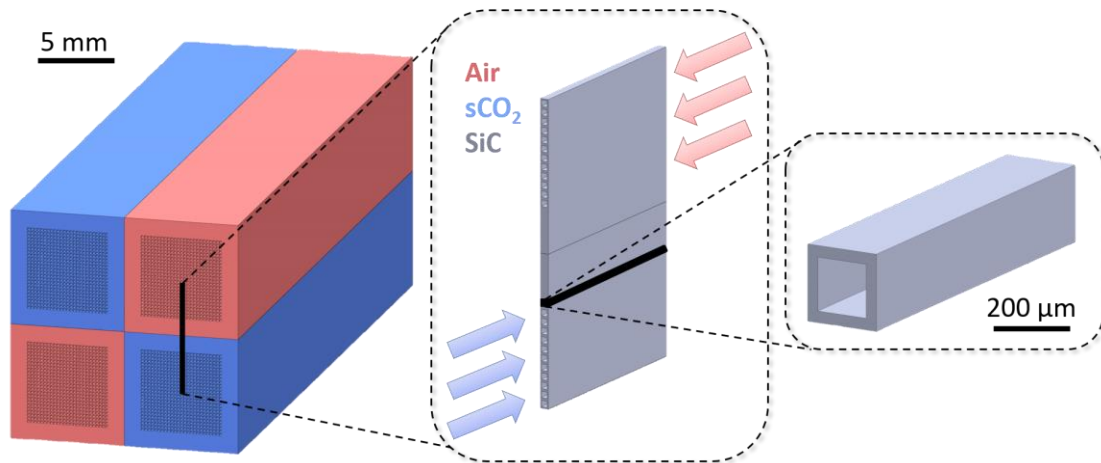
Figure 4 – Physical representation of a section of proposed heat exchanger core, assembled here in a 2 × 2 core with hot (red) and cold (blue) channels. The heat exchanger discussed in this thesis is a 6 × 6 core, with 18 hot and 18 cold macrochannels, and headers to direct the flow from the cycle to the core and back to the cycle.

Overall, this design offers several improvements to current state-of-the-art heat exchangers. Designed for a sCO$_2$ Brayton cycle, the heat exchanger efficiency benefits from high temperature, high pressure working fluid conditions. Inclusion of microchannel structures increases the heat transfer surface area to volume ratio to approximately 7100 m^2/m^3 per macrochannel in the checkerboard arrangement, surpassing ratios for similar heat exchangers listed in Table 1. For volume and mass-constrained applications like aviation, this high ratio is important. Moreover, microchannel structures provide mechanical stability to the heat exchanger core. Structural optimization of the microchannel geometry with respect to stress concentrations can be performed to meet a targeted safety factor or application. Square channels are chosen as they can be repeatably stacked and co-extruded while minimizing gaps and deformities to the structure. Fabricating the heat exchanger core using ceramic co-extrusion can enable these microchannels to be formed quickly and cost-effectively, lending to the scalability of the process. While conceptually promising, future work will include a techno-economic analysis of manufacturing via co-extrusion and provide concrete values for cost with respect to scale.

2.3.1. Material properties – literature values

Researchers from Purdue University, led by Professor Rodney Trice and Professor Jeffery Youngblood, are currently developing a custom SiC blend to meet project requirements. Initial thermal characterization of SiC material candidates was conducted and is presented in this thesis; however, some critical material metrics remain uncertain, including values for tensile strength and modulus. Structural modelling requires

accurate material properties for SiC, thus values from literature (Table 3) are used when experimental data is unavailable or not finalized. Model adjustments based on variations of these parameters are emphasized in this report and can be implemented in the future following complete material characterization.

Table 3 – Material properties for 3C-SiC (β-SiC) at room temperature [27][28]**.**

Parameter	Value	Description
E_{SiC}	345 GPa	Young's modulus, sintered
ν_{SiC}	0.18	Poisson's ratio
ρ_{SiC}	3160 kg/m^3	density
α_{SiC}	4.7×10^{-6} K^{-1}	coefficient of thermal expansion, 0-1973K
σ_{yield}	5000-9000 MPa	yield strength in compression
σ_{UTS}	350-650 MPa	yield strength in tension
K_{SiC}	2.5-4 MPa m$^{-0.5}$	fracture toughness
λ_{SiC}	100-200 W/mK	thermal conductivity
a_{SiC}	$30\text{-}100\times10^{-6}$ m^2/s	thermal diffusivity

Chapter 3

3. Structural analysis of HX core

The following chapter describes steps taken to mechanically evaluate the proposed heat exchanger design, and all optimization work that was done to ensure material survival during operation. Thermal-fluidic modelling and optimization was done in Wang *et al* [23] and was used in parallel with the following work to conclude the optimal heat exchanger design. Conclusions from the thermal-fluidic modelling can be seen in section 4.6. Overall, mechanical strength modeling centered around two key goals: identify location(s) where stress profiles in the SiC material are at a maximum, and optimize the core's geometry to mitigate these maximum stress values to avoid failure of the brittle SiC.

3.1. DEFINING STRESS IN A BRITTLE MATERIAL

When discussing strain behavior and the resulting stress profiles developed due to external loading it is essential to define what is meant by stress in the material. For a brittle material such as SiC, it has been shown that stress values of concern are 1st and 3rd principal stress values [29][28] and directly correlate to failure of the ceramic in tension or compression, respectively. Principal stress values in a finite element can be directly calculated by equation (5), whose 1st and 3rd principal stress value solutions represent a maximum and minimum, respectively. A spatially-fixed positive 1st principal stress value signifies a location of material loading in tension, while a negative 3rd principal stress value signifies a location of material loading in compression. These values, positive 1st and negative 3rd principal stress values, will therefore be directly compared to the tensile and compressive limits of SiC as listed in Table 3 throughout this analysis.

$$\sigma_{1,3} = \left(\frac{\sigma_x + \sigma_y}{2}\right) \pm \sqrt{\left(\frac{\sigma_x - \sigma_y}{2}\right)^2 + \tau_{xy}^2} \tag{5}$$

Priority is given to 1st principal stress profiles as SiC is more likely to fail in tension rather than compression when multi-axially loaded [30]. Furthermore, stress values reported are averages over small surface areas, those encompassing high- and low-pressure fillets, to provide accurate and repeatable results as discussed in section 3.3.

3.2. CLASSICAL BEAM THEORY

Channels with no internal porous structures, and fixed end conditions, were analyzed to quickly visualize stress on the channel walls using classical Euler–Bernoulli beam theory [31] as shown in Figure 5. While this analysis is useful for easily determining stress trends with respect to geometry parameters, the values

themselves are lower than expected due to the fixed-fixed end conditions. As shown in future sections, the channel walls are not fixed and instead deformation about the corners is compounded by adjacent walls. However, some insights into the mechanical response to pressure loading in the proposed manner can be taken from a beam theory analysis.
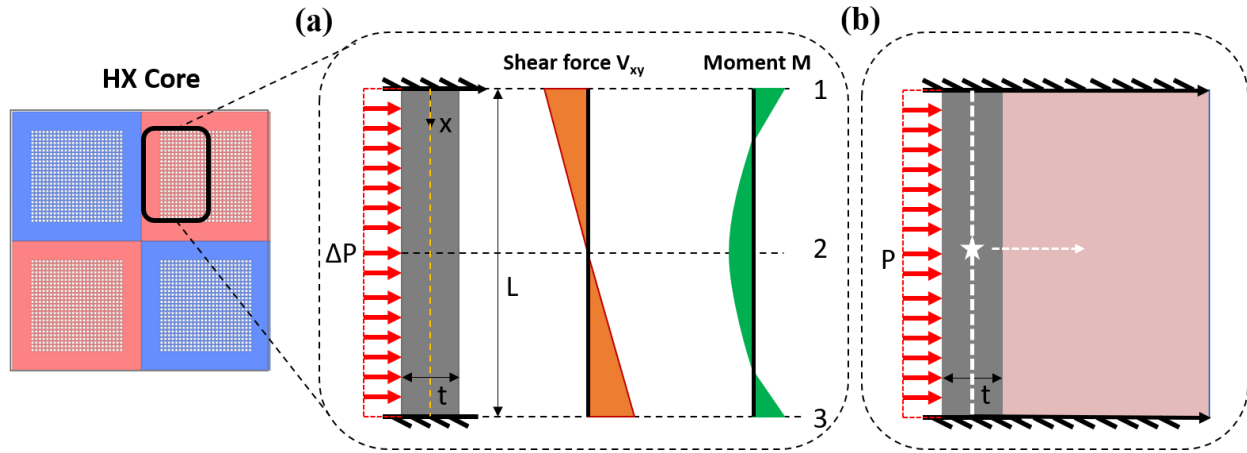
Figure 5 – (a) Simplified channel wall geometry with uniform pressure loading and resulting shear, moment diagrams. (b) Centroid of the beam translates horizontally in response to the addition of porous support material internal to the channel.

The simplified fixed-fixed beam situation produces a stress profile with max values that trend with equation (6),

$$\sigma_{max} = \frac{My}{I} = \frac{\frac{M_1 t}{2}}{\frac{wt^3}{12}} = \frac{L^2 P}{2t^2} \tag{6}$$

where P is the pressure differential between the two temperature-opposing channels (170 bar). Several conclusions can be drawn from this simple relationship, including the significance of the corner locations. Maximum stress in the β-SiC is located at the corners labeled 1 and 3 in Figure 5. Later mechanical simulations will thus focus on these areas of interest when evaluating 1st principal stress magnitudes. Furthermore, equation (6) demonstrates that stress has an inverse dependence on the moment of inertia I and thus identifies thickness t as an impactful parameter when optimizing to mitigate stress concentrations. Dependency on the presence and density of microchannels internal to each macrochannel can also be observed. In this periodic system, consisting of one wall and half the area internal to a macrochannel, the centroid location that determines I depends on macrochannel wall thickness and the density of the interior material. For the wall alone, the neutral axis stays fixed at the middle of the wall, and beam theory predicts that thickness quadratically decreases maximum stress in the corner. However, the interior microchannel

structure is also resisting deformation and therefore must be factored into the maximum stress calculation. As this effective porosity is taken into account, and the system now includes both the wall and the interior material, the centroid moves right horizontally from the centerline of the wall. Because the length scale of the porous structure is significantly larger than that of the wall, small changes in wall thickness ($\pm$ 1mm) may no longer significantly change the location of the centroid. This hypothesis is validated in the next section as the reason for the lack of dependency on wall thickness with respect to maximum bending stress at low porosities.

3.3. COMSOL MODEL

Transitioning from a simplified view of the strength analysis to the actual heat exchanger core geometry, COMSOL Multiphysics v. 5.5 was used to develop a framework for finite element analysis (FEA) of the actual proposed system. All computational models presented in this work, unless otherwise stated, were modeled using COMSOL. Mesh refinement studies were run for all scenarios to ensure convergence and give confidence in the results prior to interpretation, an example of which is shown in Figure 6. Although the initial design includes sharp 90° corners in both macrochannels and microchannels, all corners are filleted to ~ 10 μm, a feature length scale on the same order of magnitude as expected grain size. Unrealistic sharp corners can lead to infinite stress concentration results in an FEA model, which are not accurate [32]. To avoid any non-physical singularities in the results, fillet-averaged stress values are primarily used in this analysis, therefore providing realistic values for stress concentrations that can impact the mechanical stability of the structure.
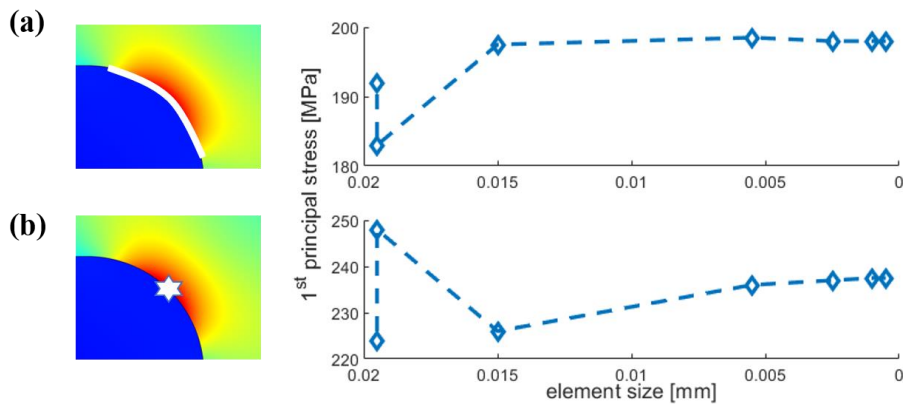
Figure 6 – Example mesh refinement study to ensure avoidance of stress singularities. Meshes whose element size in filleted corners was less than 0.006 mm yielded consistent values ($\leq$ 0.01% variation) for both fillet-averaged stress (a) and maximum stress (b).

3.3.1. Porous media model

A four-channel heat exchanger structure was evaluated with periodic boundary conditions to fully capture the pressure differentials and resulting stress profiles of the proposed heat exchanger design, while reducing the computation time required. Equation (7) shows how to transition from actual microchannel size to an effective porosity used in simulations,

$$\varphi = 1 - \frac{a_{micro}^2 - (a_{micro} - 2t_{micro})^2}{a_{micro}^2} \tag{7}$$

where a_{micro} is the side length of a single square microchannel structure (fixed at 200 µm) and t_{micro} is the microchannel wall thickness. Elastic material physics and first principal stress values are used in all COMSOL simulation results, and periodic conditions are applied to all outer edges in Figure 7. The mechanical simulations here are done under ambient temperature conditions, with pressure values of 250 bar and 80 bar acting on the internal cold and hot macrochannel wall boundaries, respectively. Fluid pressure was taken as the only stress-inducing mechanism in the core, assumed to be independent of temperature. Young's modulus values for the porous microchannels are approximated using a linear relationship between modulus and porosity first developed by Pabst et. al. [33], shown in equation (8). Validation of these assumptions using a microchannel array model is performed in the following section.

$$E_{porous} = E_{SiC}(1 - \varphi)\left(1 - \frac{\varphi}{0.684}\right) \tag{8}$$
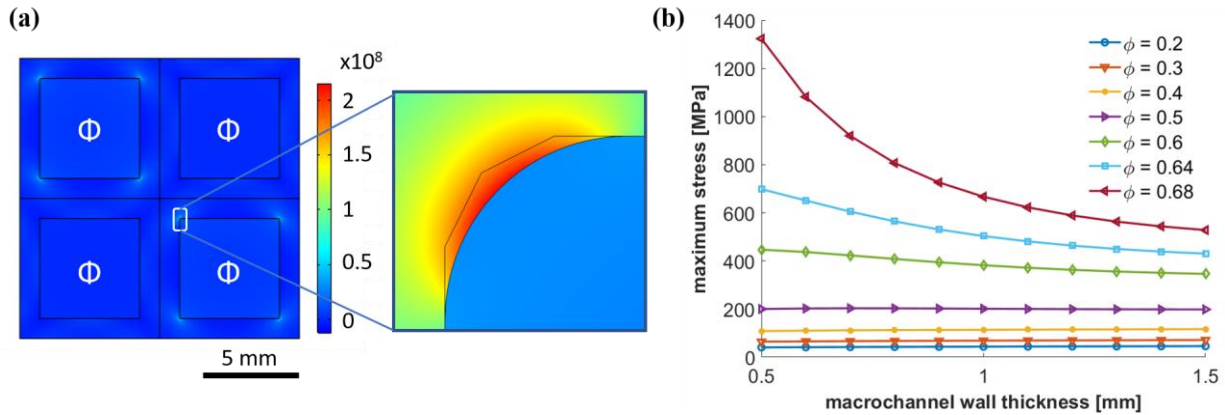
Figure 7 – 1st principal stress values in the SiC core, consisting of two hot and two cold channels with periodic boundary conditions applied, with respect to macrochannel wall thickness. Maximum values were taken as averages over the fillet area bounded by the blue polynomial (a) and plotted as a function of macrochannel wall thickness and porosity ϕ (b). Wall thickness does not significantly impact stress values at the target porosity of 50%, as hypothesized by 1D beam theory.

An empty channel under uniform pressure loads exhibits a maximum 1st principal stress value of ~700 MPa given a wall thickness of 1 mm. Modification of an empty channel is clearly required, because without the support of microchannels this maximum stress concentration far exceeds the tensile strength of SiC (~500 MPa) [33]. Therefore, the porous structure (microchannel network) is essential to maintain the structural integrity of the heat exchanger core. At 50% porosity, as proposed by the thermal-fluidic analysis [23] the maximum tensile stress value is approximately 200 MPa, yielding a safety factor of 2.5 against mechanical failure compared to literature.

3.3.2. Justification for use of porous media model

A porous media approximation for the microchannel arrays was implemented in section 3.3.1 to ease computational demands while maintaining adequate mesh densities for accurate FEA, and has precedence in the literature [34]. A computationally intensive multiscale model, featuring microchannel walls instead of the porous media approximation, is used in Figure 8 to provide justification for the porous approximation when applied to mechanical evaluations. Every microchannel wall is loaded with the static pressure of the operating fluid (80 bar and 250 bar of the hot and cold side, respectively) with symmetry conditions on all border edges and a fixed point in the center to calculate a unique solution. Fillets on each microchannel corner shown in Figure 8a are the same as in the porous media model (10 μm) and have similar element densities as well. Working fluid material within each microchannel (air and sCO_2) is assumed to provide no resistance to structural deformation. 1st principal stress values experienced by the HX core over length scales equivalent to the microchannel features are shown in Figure 8b to match those in the porous media model (Figure 7). Both the lack of dependency on macrochannel wall thickness at low microchannel wall thicknesses (porosities) and the significance of microchannel wall thickness (porosity) on 1st principal stress values are featured in Figure 7b and Figure 8b. In this way we can ensure the accuracy of our porous media simplification. With a tensile limit of ~500 MPa, SiC microchannel walls will not fast fracture under current pressure-loading conditions, as marked by a star in Figure 8b (~200 MPa).
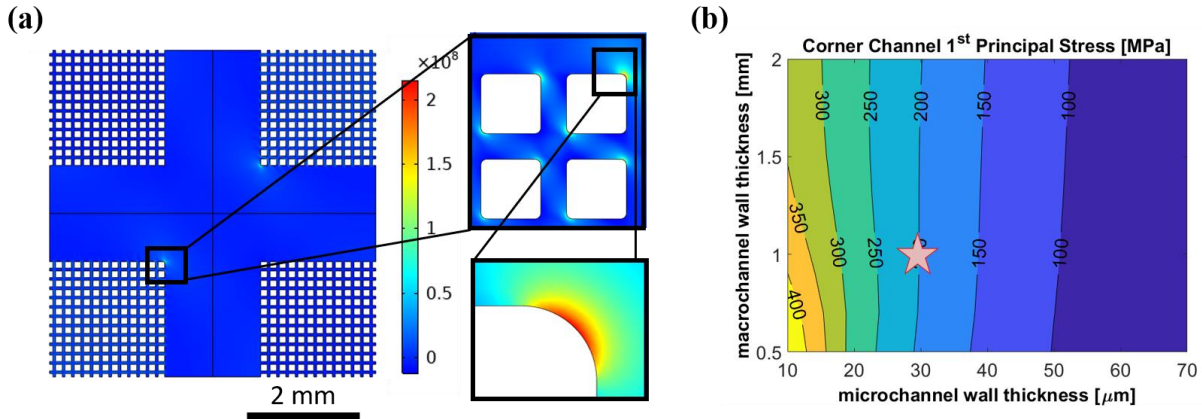
Figure 8 - Structural analysis of the microchannel heat exchanger core using COMSOL (a). Four quarter macrochannels are simulated, two air and two sCO₂ assembled in a checkerboard pattern. (b) Overall 1ˢᵗ principal stress concentrations in the high-pressure fillets match those presented in Figure 7.

3.4. RESULTS BASED ON DESIRED PERFORMANCE GEOMETRY

3.4.1. Thermal expansion considerations

Proposed working fluid inlet conditions, air at 1285 °C, 80 bar and sCO₂ at 300 °C, 250 bar, have the potential to create significant thermal stresses within the HX core. To assess this scenario, thermal data was first taken from thermal fluidic simulations [23], summarized in Figure 9. A 3-dimensional thermal-fluidic model in Figure 9a provides thermal data for the entirety of the heat exchanger core, which was then averaged by working fluid in Figure 9b to shown temperature as a function of distance along the core. Four distances measured from the sCO₂ inlet (0.0 cm, 0.7 cm, 2.1 cm, and 4.0 cm) were specified as cross-sectional slices to analyze structurally. Temperature values and their corresponding parabolic temperature profiles from each slice were implemented into a structural simulation of the entire 6×6 HX core and a parametric sweep was performed to determine 1ˢᵗ principal stress values over a variety of thermal cross-sections. Results of this parametric sweep are shown in Figure 10. A previous study on the high-temperature strength of pressureless-sintered SiC [35] has demonstrated a negligible dependence on temperature up to 1000 °C, with only a 9% decrease in flexural strength up to 1200 °C. Therefore, room temperature failure strength values are used for upper limit thresholds in all models, regardless of operating temperature.

28
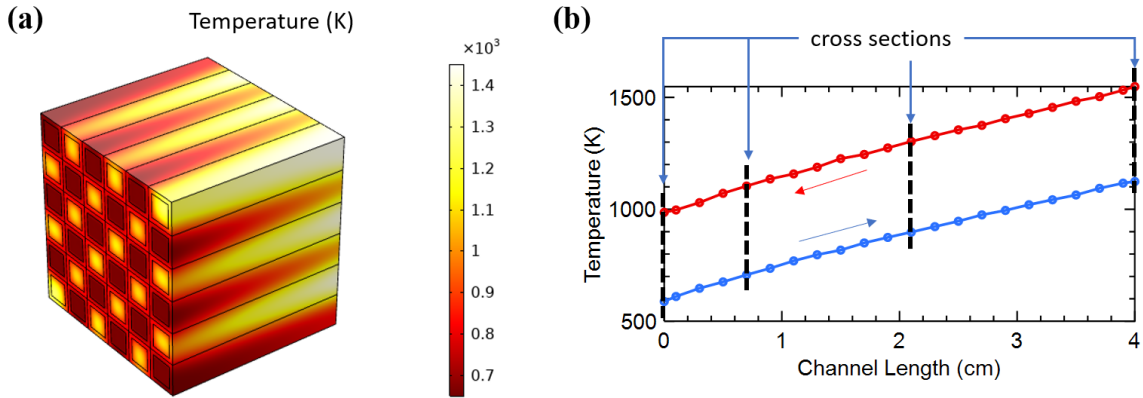
Figure 9 – (a) Thermal simulation results of an entire 6 × 6 HX core with air and sCO₂ at operating conditions. (b) Four cross-sectional cuts of data were taken for average temperature along the length of the HX core, represented by black dashed lines. Blue data points are values associated with sCO₂ while red are air data points.
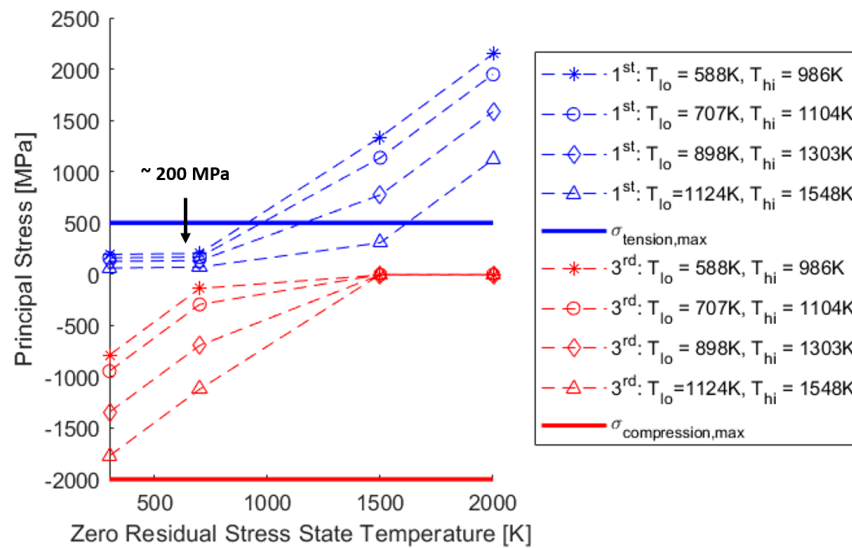
Figure 10 – Structural simulation results that include both pressure loading and thermal stress mechanisms. Temperature values reflect those in Figure 9 for each of the four slices. All perimeter boundaries are under a free condition. 1ˢᵗ principal stress values (blue) and 3ʳᵈ principal stress values (red) were taken as surface averages over the region near the fillet of a high pressure and low pressure macrochannel, respectively. For a residual stress state temperature of 300-700 K, 1ˢᵗ principal stress values reflect those found in ambient temperature simulations.

Zero residual stress state temperature is defined in these models as the temperature at which the SiC material is under no thermal loading. This temperature is highly dependent on the manufacturing process, and

heating/cooling steps can be adjusted to achieve various values. For a residual stress state temperature of 300 – 700 K, 1st principal stress values match those in the pressure loading only simulations, while 3rd principal stress concentrations have the potential to be significant. If the HX core was fixed on all external faces this compressive stress would be magnified, hence the need for free boundary conditions along the perimeter. As modelled, a residual stress state temperature of 700 K will yield a safety factor of 2.5 for failure in tension and 2 for failure in compression compared to literature values in Table 3. Further work by our collaborators at Purdue University will provide estimates for expected zero residual stress state temperature and lead to model improvement.

In summary, several geometric and design parameters have been identified as variables that impact principal stress values in the HX core and are qualitatively represented in Figure 11. This image highlights the effect various parameters have on both the maximum 1st and 3rd principal stress values. The black star represents a common core geometry as set by thermal-fluidic simulations, consisting of microchannel arrays that are equivalent to 50% porosity, 1 mm wall cladding, a macrochannel internal fillet of 10 μm, a zero residual stress state temperature of 300 K and free boundary conditions. By changing one parameter all others are assumed constant. If we were to increase the residual stress state temperature the maximum 3rd principal stress would go down, but the 1st principal stress would increase. If instead the boundaries were fixed, both maximum principal stresses would increase. If we were to increase the cladding thickness of each macrochannel, neither value would fluctuate significantly. If the effective porosity of the microchannel arrays internal to each macrochannel were to decrease, 1st stress values would decrease but with the penalty of increasing 3rd. Finally, if the internal fillet size of each macrochannel was to increase the core would experience a sharp decrease in the maximum 1st principal stress values without significantly varying the 3rd principal stress maximum. This simplified summary of parameter trends will be used in the future as we learn more about our material and manufacturing process to address potential concerns about the strength of the design.
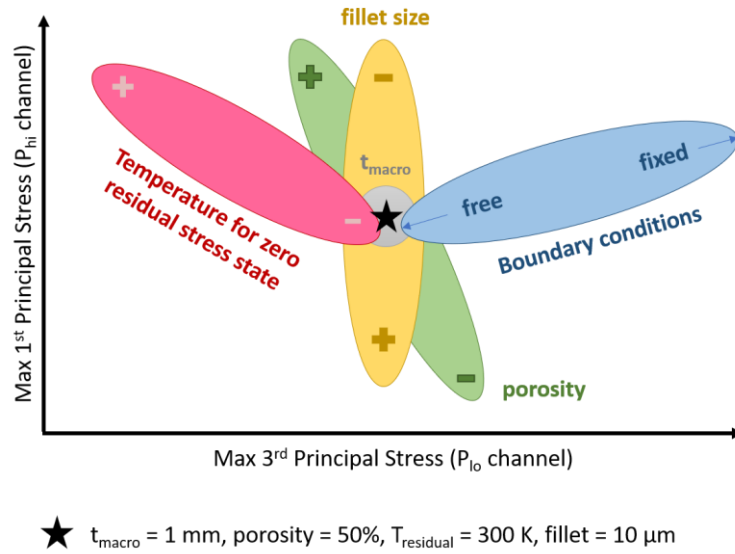
Figure 11 – Abstract representation describing how varying certain parameters will impact the 1st and 3rd principal stress values experienced in a checkerboard HX core.

3.5. FAILURE ANALYSIS

A framework for evaluating the structural survival of a material analytically is done using Griffith's Crack Criterion [36][37], shown in equation (9),

$$\sigma_f = \frac{K_C}{\sqrt{\pi a}} \tag{9}$$

where a is the crack length and K_C is the critical stress intensity factor, sometimes referred to as the fracture toughness of the material. Defects and grain boundaries serve as nucleation sites for cracks and statistically vary in size, therefore a range of possible fracture toughness values for SiC are plotted in Figure 12 with respect to defect size.

3.5.1. Estimates based on COMSOL model

Acceptable ranges for grain sizes and defects are estimated using equation (9) and 1st principal stress values from Figure 7 (200 MPa). Results are plotted in Figure 12. To avoid fast fracture in the solid SiC macrochannel walls, where a 200 MPa tensile stress develops, crack lengths must be below 50 – 130 μm. Given our co-extrusion manufacturing method the solid SiC is expected to have grain sizes on the order of 1 – 2 μm [38]. Therefore, it is reasonable to expect material survival if defect sizes can be kept below this

critical threshold. Further analysis and testing are required to determine the impact of cyclic loading on sub-critical crack growth and potential lifetime limits of the SiC.
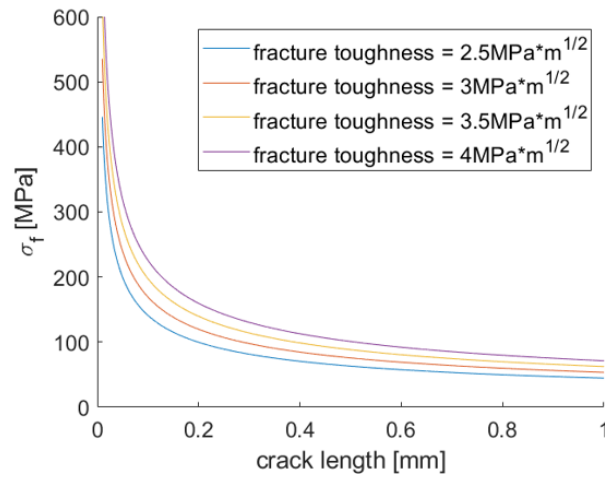
Figure 12 – Critical 1ˢᵗ principal stress values that will lead to crack propagation and thus material failure for crack lengths 0 to 1 mm. Cracks and defects larger than 50-130 μm in the solid SiC macrochannel walls (Figure 7) are predicted to cause fast-fracture and thus failure of the SiC heat exchanger.

3.6. ADJUSTMENTS DUE TO MANUFACTURING DEFECTS

All conclusions and solutions thus far have been done assuming an ideal SiC material whose properties reflect those listed in Table 3. However, because of our pressureless-sintering methodology for heat exchanger fabrication, residual porosity after green-body densification has the potential to drastically effect mechanical strength of SiC [39]. Typical solutions for this phenomena, such as sintering under pressure [40] or densifying the green-body using pressure prior to sintering [41], cannot be done without collapsing the microchannel structures. Therefore, mechanical strength values lower than that initially reported in Table 3 are to be expected. While this strength reduction can be mitigated using non-pressure-loading techniques, such as adjustments to the additives and sintering temperatures, initial mechanical testing has been done and reported by our collaborators at Purdue University listing sample tensile strengths of dense SiC as ~120 - 140 MPa. Significant design adaptations are required to accommodate this lower tensile strength for our target application, several of which are presented here. First principal stress maximums for the previous core architecture are repeated in Figure 13a, while Figure 13b, c present 1ˢᵗ principal stress maximums for alternating open and closed microchannel architectures as a function of macrochannel and microchannel wall thickness. Current design parameters of 1 mm macrochannel wall and 30 μm microchannel wall are highlighted in red. Figure 13d shows how microchannels can be arrayed with

32

alternating open and closed extrudates to reduce 1st principal stress concentrations in the filleted corners from 200 MPa to 100 MPa. In theory this strategy does not increase the complexity of the manufacturing process, although it may impact thermal performance of the heat exchanger core.
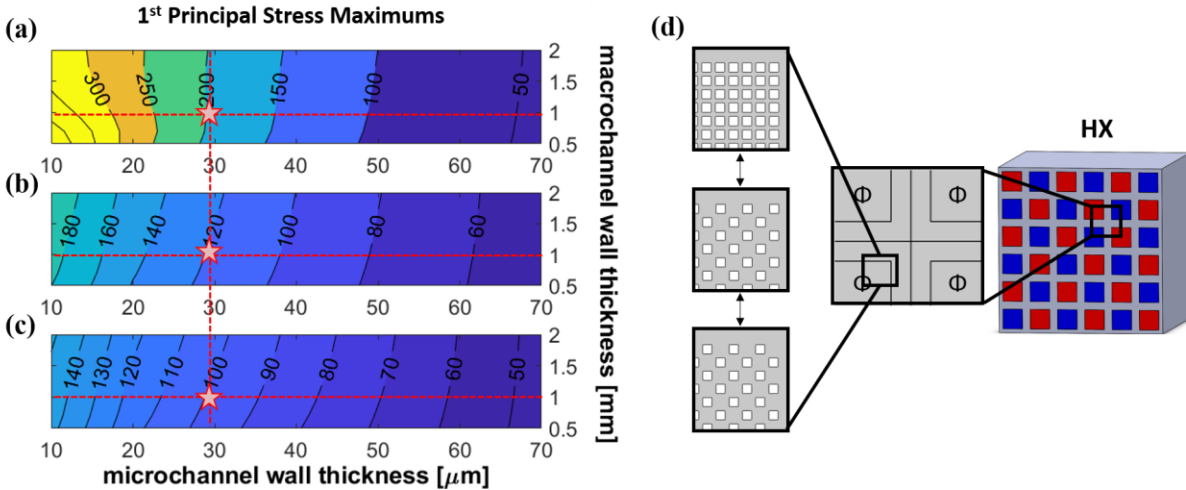
Figure 13 – Alternating open and closed microchannels to decrease 1st principal stress profiles in the HX core. 1st principal stress maximums with respect to macrochannel and microchannel wall thicknesses are plotted for each of the three arrangements: (a) originally proposed design, (b) alternating closed microchannels starting with the corner open, and (c) alternating closed microchannels starting with the corner closed. Red stars mark the previously targeted geometry. (d) Visualization of design variations.

Impacts of these solutions to performance metrics will need to be evaluated prior to finalizing a design. While no one solution has been determined as of this publication, flexible options will allow for future work to adapt quickly to the needs of our manufacturing partners and applications.

3.7. OVERALL HX CORE PERFORMANCE

Thermal performance of the heat exchanger core was done by Wang *et al* [23] and is summarized as follows: With air and sCO$_2$ as working flows (0.08 kg/s) in aviation applications, this proposed design can achieve a volume specific UA of 1.4 MW/K/m^3 with the proposed geometry. The heat exchanger core achieves a power density of over 700 MW/m^3, 300 kW/kg with 50% thermal effectiveness, or 10.3 MW/m^3, 4.3 kW/kg with 95% thermal effectiveness, while maintaining a pressure drop lower than 1.5%.

Chapter 4

4. Design optimization of heat exchanger headers

4.1. OVERVIEW OF HEAT EXCHANGER HEADERS

Headers are components of the heat exchanger assembly responsible for directing flows from the cycle to the core (inlet headers) and from the core back to the cycle (outlet headers). As previously proposed, the heat exchanger core consists of 18 hot and 18 cold macrochannels arranged in a checkerboard pattern. This arrangement, paired with the manufacturing limitations of SiC, poses significant difficulties for designing inlet and outlet headers. Previous solutions to manifolding a checkerboard heat exchanger core have relied on machining complex geometries into metal and/or shearing the metal core layers to transition to a plate-type heat exchanger at the ends [42], strategies which are unavailable due to the brittle behavior of SiC. Therefore, novel subcomponent designs for directing flow into and out of the heat exchanger core had to be developed. Analysis of a proposed header design is done to evaluate five interconnected goals: feasible from a manufacturing standpoint, achieving a safety factor against mechanical failure, minimal viscous pressure losses, uniform distribution of fluid, and capability of being fixed to the HX core and cycle tubing. The final header design is presented in this report.

4.1.1. Important considerations for header design

First order performance estimates are essential for iterating through designs of compact heat exchanger headers, while complex numerical models are used to finalize metrics for a chosen design [43]. The header system features two distinct subsystems: a hot inlet and outlet, parallel to the flow within the HX core, and a cold inlet and outlet, perpendicular to the HX core. This cold-side header can be identified as the most complex subcomponent fluidically and thus is the focus of header optimization work. Because sCO_2 is the higher-pressure working fluid, it was selected to be the fluid interacting with the more restrictive header (see Figure 14). This allows for a lower percentage pressure change compared to the air working fluid in a similar geometry, given a constant value for viscous pressure losses. Initially, two approaches to header optimization were defined: a header that was ideal from a performance standpoint, and one that was preferable from a manufacturing standpoint. These two criteria were discussed with our collaborators at Purdue University and used to develop the optimal header design presented here. Currently, fabrication of the header subcomponents is limited to injection molding [44] and machining, the former used for large non-precise parts and the latter used to make complex features such as the sCO_2 channels. By machining the critical channels directly into the heat exchanger core extrudate we remove any issues associated with

mismatch and co-sintering, reducing the complexity of the heat exchanger. It is this channel width that was varied to achieve minimal pressure losses and maximal flow distribution.

Headers are computationally evaluated via two main criteria: flow maldistribution and irreversible pressure losses [45]. Flow maldistribution, mainly related to the construction of the header, negatively impacts the effectiveness of a heat exchanger [46] and thus should be mitigated during the header selection process. For fully constrained flow in a heat exchanger, it is common to use a mass maldistribution parameter S,

$$S = \sqrt{\frac{1}{n-1}\sum_{i=1}^{n}(\dot{m}_i - \bar{m})^2} \tag{10}$$

where n is the number of outlet channels (18) and $\dot{m}_i$ is the mass flow rate for respective outlet channels [47]. Furthermore, irreversible pressure losses, also known as viscous losses or minor losses in piping systems, govern pump power requirements for the overall cycle and thus should be minimized. Due to the complexity of the heat exchanger geometry a computational model factoring in viscous dissipation and eddy formation was not feasible. However, first order approximations for irreversible pressure losses are done using a common pipe flow analogy. An analysis of this approximation is shown in section 4.2.1.2.

4.2. FINAL DESIGN

The inlet and outlet sCO_2 headers are rotated $45°$ with respect to the core to better guide the inlet flows into inner macrochannels. Two inlets rather than one are used for the sCO_2 as it decreases the distance, and thus the frictional losses, between inlet and center macrochannels. Both of these strategies improve the performance without affecting the manufacturing complexity of the header subsystem. Figure 14 shows an exploded view of the entire heat exchanger assembly, including both working fluid headers and the HX core. Multiple parts are necessary to reduce manufacturing complexity, because while simple SiC parts are often joined to one another it is difficult to produce an individually complex part. Methods for interfacing header components include co-sintering and diffusion bonding, both of which are currently being pursued by our collaborators at Purdue. Air and sCO_2 headers both start with a circular-to-square loft piece to facilitate standard connections with cycle tubing. Additionally, the sCO_2 header has a plate component that blocks air from mixing with sCO_2 and a channel component that is machined directly into the HX core to allow for sCO_2 to reach the internal macrochannels.
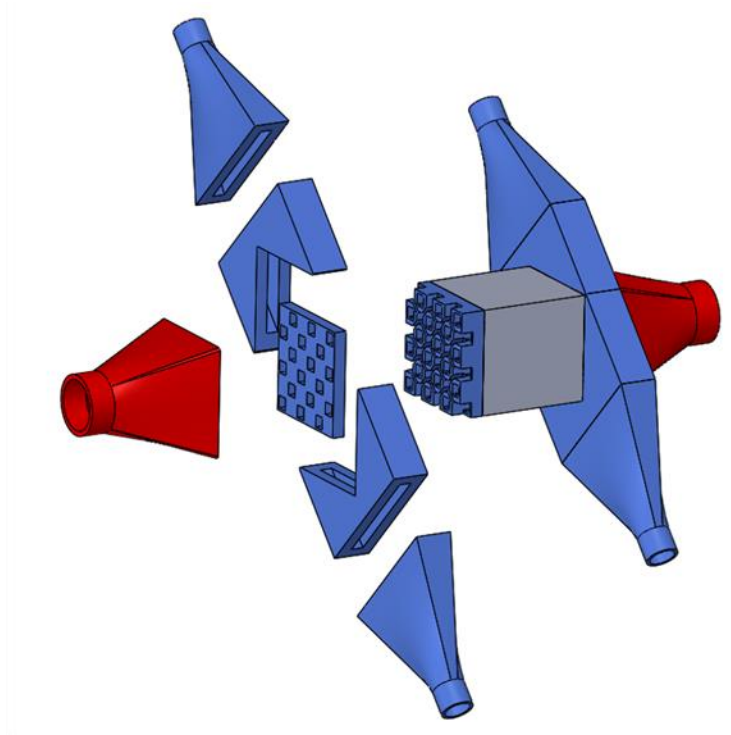
Figure 14 - Exploded view of heat exchanger component, highlighting hot (red) air and cold (blue) sCO₂ headers. All components shown here are SiC.

Figure 15 demonstrates how the sCO$_2$ header components were translated to working fluid domains in COMSOL, with the critical header subcomponent detailed in Figure 16. This critical piece is responsible for directing fluid from cycle inlets to the macrochannels and will be machined directly into the heat exchanger core to improve part tolerance and reduce the total number of header components. It is this sCO$_2$ header subcomponent that is subject to optimization in the following section. Depth L of the sCO$_2$ header does not significantly impact either mass distribution nor pressure losses and is thus set at 5 mm to allow for common endmills to be used (a 1 mm endmill typically has a cutting depth of ~ 5 mm). Overall width is fixed at 42 mm to match the core, as are parameters a_{macro} and t_{macro}. Width of the channels milled into the core, denoted *channel*, is the driving parameter for optimization of the sCO$_2$ header design.
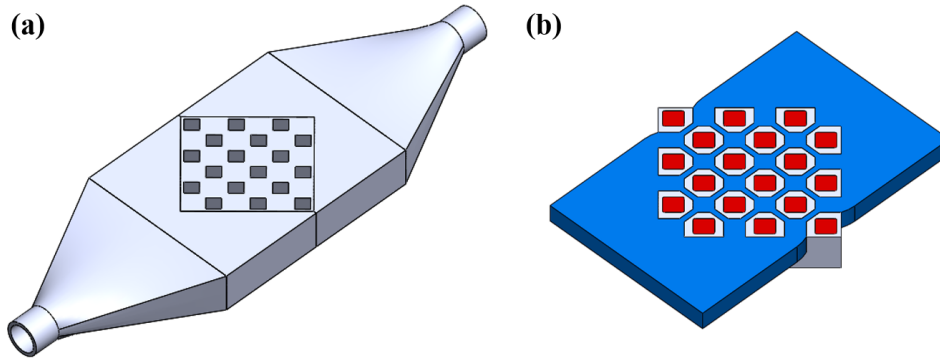
Figure 15 – (a) sCO₂ header subsystem, made of SiC. (b) Fluids/structures modelled in COMSOL. Blue regions represent sCO₂, red regions stand for air, and grey regions are SiC.
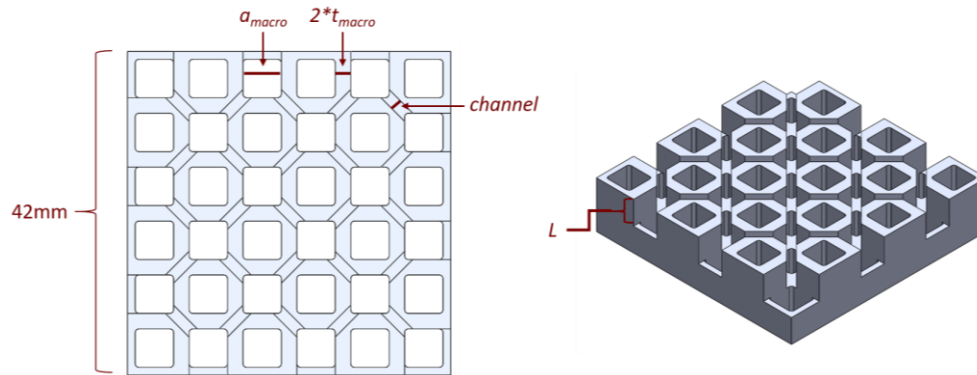
Figure 16 – sCO₂ header subcomponent is formed by machining the heat exchanger core. The channel width and height can be varied for the optimization of pressure drop and mass distribution. Core parameters a_{macro} and t_{macro} are determined by the analysis in section 3.3.

Preliminary dimensions for sCO₂ header subcomponents whose geometries do not affect performance and are therefore contingent solely on their manufacturability are shown in Figure 17. Thus far, the only criteria imposed on these components are: long enough to avoid flow separation (~50 mm), capable of cycle connections (square-to-round loft), and sufficiently thick to avoid material failure (5 mm). Parts shown in Figure 17a and b are distinct to reduce the size of the cycle connection piece, thus improving the likelihood of successful fabrication using injection molding. Furthermore, given its rectangular size and through-cut features, a standard mill can theoretically produce part c from stock material. The remainder of this section focuses on the geometric optimization of the critical subcomponent identified in Figure 16 and the overall performance evaluation of both air and sCO₂ headers.
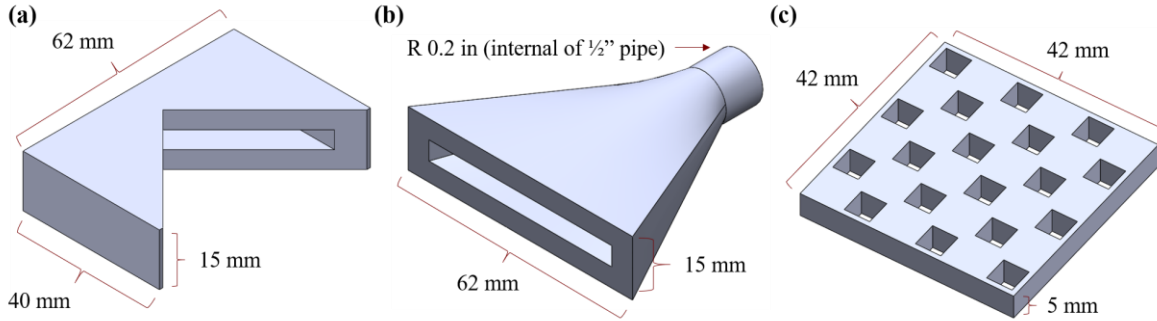
Figure 17 – Fixtures for the sCO₂ header, whose geometries are dictated solely by manufacturability and therefore subject to change. Preliminary dimensions are shown, allowing for fixtures to connect to cycle tubing while providing sufficient mechanical strength to avoid failure (5 mm thickness). (a) inlet to HX core connector, (b) cycle inlet to rectangular inlet, (c) blocker plate to separate air and sCO₂.

4.2.1. Fluidic performance

4.2.1.1.   Flow maldistribution

Fluid domain shown in Figure 18 was simulated in COMSOL under the following guidelines: symmetric boundaries both vertically and horizontally, mass flux of 0.04 kg/s per inlet, incompressible flows with an inviscid flow assumption, and an outlet condition of 0 Pa. Conservation of mass and momentum were the governing equations, and the inviscid flow assumption drastically reduced computational resource demand. This assumption was justified as follows. For time-averaged turbulent boundary-layer flow, equation (11) scaling applies, derived from equating the advective and viscous terms in the steady-flow momentum equation for surface-parallel velocity component [48],

$$\frac{\bar{\delta}}{D_h} \sim \frac{1}{\sqrt{Re}} \tag{11}$$

where δ is the boundary layer thickness and D_h is the hydraulic diameter. With a given mass flux of 0.04 kg/s per inlet, $\frac{\bar{\delta}}{D_h} \sim 0.005 \ll 1$ at the first opening for a macrochannel and $\frac{\bar{\delta}}{D_h} \sim 0.0035 \ll 1$ in the header channel. This validates the inviscid assumption for this model due to the negligible potential for skin friction/viscous dissipation given insignificant boundary layer thicknesses.

Results from the inviscid flow COMSOL simulations are shown in Figure 18, indicating significant reduction in flow maldistribution parameter S for channel widths at or above 1.5 mm. A maldistribution S of 6 g/s, with a channel width of 1.5 mm, proves to be acceptable for current state-of-the-art headers with

a negligible effect on heat exchanger core performance [45]. Channels larger than 1.5 mm are possible but may reduce the mechanical strength of the header and will require tighter tolerances on channel fabrication. These drawbacks are coupled with a small (2 g/s) decrease flow maldistribution for larger channels, thus a channel width of 1.5 mm is recommended. A similar COMSOL simulation was done for the air header, varying overall length to achieve uniform mass distribution into the HX core. Due to the direct, momentum-driven nature of the air flow, this desired length corresponds to the length where flow separation from the walls is minimal. A drastic drop in flow maldistribution degree S occurs at a length of 50 mm in Figure 19, signaling a reduction in flow separation. Increasing the length of the air header over 50 mm only marginally improves flow distribution while significantly reducing the mass- and volume-based energy densities of the heat exchanger. Therefore, 50 mm is the target length for the air header.
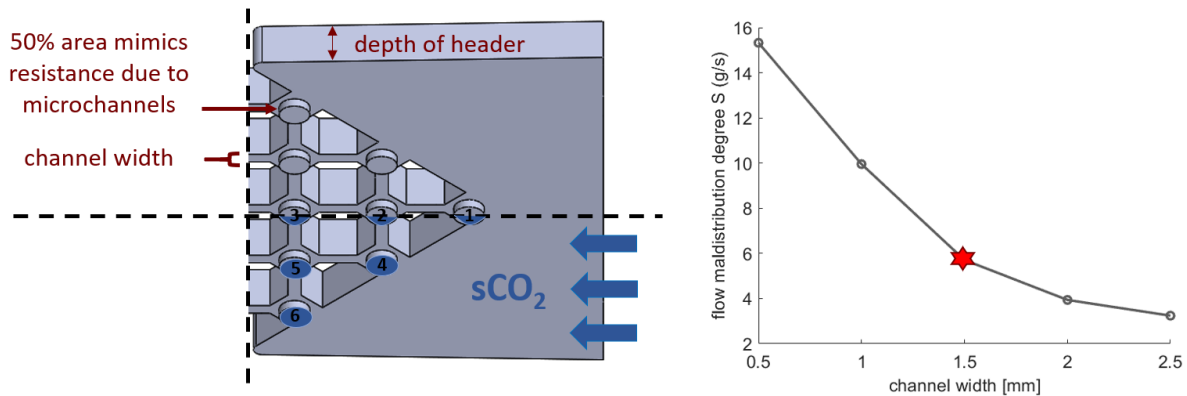
Figure 18 – sCO₂ fluid (grey) simulated in COMSOL. Parameters varied during the optimization process are labeled as red. Depth of header was found to have a minimal impact on flow distribution, while the channel width is dominant. A channel of 1.5 mm provides adequate flow distribution without sacrificing structural integrity.
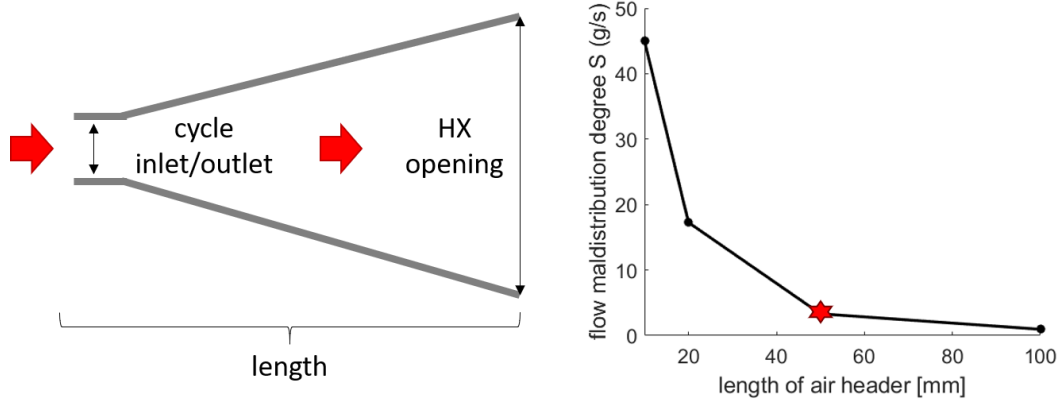
**Figure 19 – Air header simulation results for mass distribution. Cycle inlet/outlet is fixed at 0.2"
diameter, and HX opening is fixed at 42 mm. Length is varied to avoid flow separation from the walls
and thus achieve adequate flow maldistribution degree S (3 g/s at length = 50 mm).**

4.2.1.2. Irreversible pressure losses

Inviscid flow mechanics are valid for analyzing the mass distribution of a fluid in a header given the
negligible size of boundary layers. However, a slight amount of energy will still be lost due to viscous
dissipation. These small losses, also known as irreversible pressure losses in the system, will increase the
pumping power required to operate the heat exchanger and therefore must be quantified. Given the
geometric complexity of the fully-enclosed header, using a no-slip turbulence model [49] to evaluate the
pressure loss is not practical. Such a model would demand excessive computational resources and is
governed by solution strategies that vary widely for such enclosed surfaces. Also, there are existing semi-
empirical approaches that have been experimentally validated for various fluids and operating conditions
and are widely accepted in industry today. K-factor loss is one such method to empirically quantify the
pressure loss due to viscous effects in a fluid flow and is commonly applied to piping systems. By relating
the longest streamlines in the header to an analogous pipe flow system, we can estimate the maximum
pressure drop in each header subsystem. Equations (12) and (13) are used to correlate pressure loss in both
air and sCO$_2$ headers using non-dimensional K factors [50][51]. K factor values are empirically estimated
based on pipe geometry and friction factor f, which is related to Reynolds number using a Blasius correlation
in turbulent pipe flow [52],

$$\Delta P = K \frac{\rho V^2}{2} \tag{12}$$

$$f = \frac{0.316}{Re^{0.25}} \tag{13}$$

where ρ is density, V is the flows average velocity (m/s), and Re is the Reynolds number [53].

Table 4 - K factor functions and qualifying criteria [50] for pressure drop analysis with an analogous pipe flow.

Geometry	Qualifying Criteria	K Factor Function
Square reduction	$Re > 2500$	$K = (0.6 + 0.48f_1)(\frac{D_1}{D_2})^2 \left[(\frac{D_1}{D_2})^2 - 1\right]$
Tapered reduction	$45 < \theta < 180$	$K = (0.6 + 0.48f_1)(\frac{D_1}{D_2})^2 \left[(\frac{D_1}{D_2})^2 - 1\right]\sqrt{\sin\frac{\theta}{2}}$
	$\theta < 45$	$K = (0.6 + 0.48f_1)(\frac{D_1}{D_2})^2 \left[(\frac{D_1}{D_2})^2 - 1\right]1.6\sin\frac{\theta}{2}$
Square expansion	$Re > 4000$	$K = (1 + 0.8f_1)\left[1 - (\frac{D_1}{D_2})^2\right]^2$
Tapered expansion	$\theta > 45$	$K = (1 + 0.8f_1)\left[1 - (\frac{D_1}{D_2})^2\right]^2$
	$\theta < 45$	$K = (1 + 0.8f_1)\left[1 - (\frac{D_1}{D_2})^2\right]^2 2.6\sin\frac{\theta}{2}$

Translation between actual header geometry and the analogous pipe flow system for both sCO_2 and air headers are shown in Figure 20 and Figure 21 respectively, where rectangular cross-sections are equated to circular pipes using equivalent hydraulic diameters. Each analogy uses the longest streamline in the header as the flow through the pipe because it experiences the largest pressure loss and thus determines the overall pumping power required for the system. The impact of channel width on pressure losses in the sCO_2 headers is conveyed in Figure 22, validating the decision to use 1.5 mm channels rather than 0.5 mm, 1 mm channels.
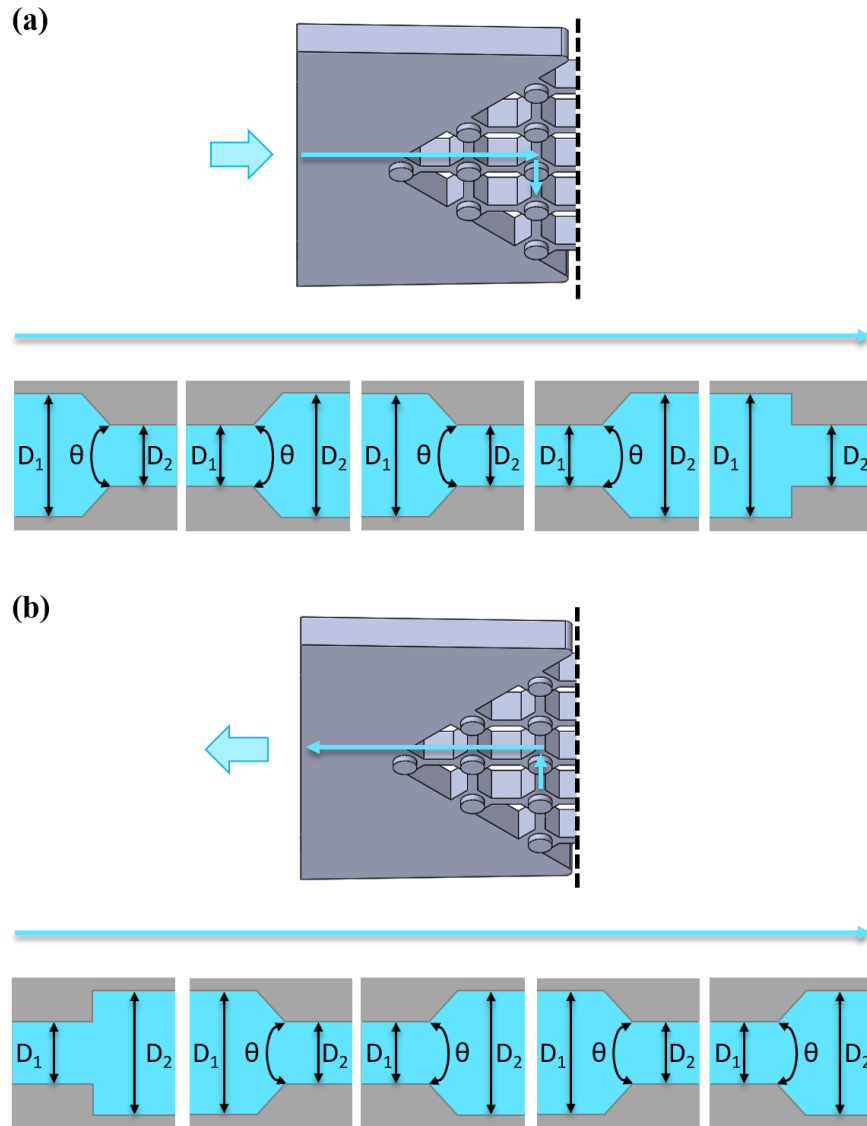
Figure 20 - Longest streamline within the sCO₂ header, translated to pipe flow using expansion and reduction K factors for pressure drop calculations. Displayed are both (a) inlet and (b) outlet single streamlines due to symmetry in the sCO₂ headers. sCO₂ working fluid is represented by grey regions in the header structure, and represented by blue in the pipe flow relationship. Total irreversible pressure drop within sCO₂ headers is calculated to be less than 0.1%.
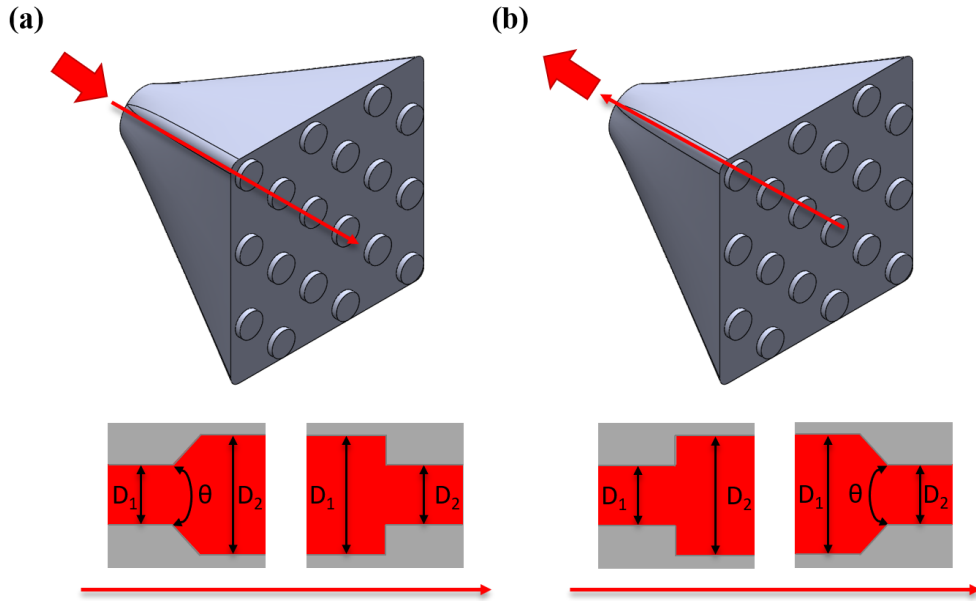
Figure 21 - Longest streamline within the air header, translated to pipe flow using expansion and reduction K factors for pressure drop calculations. Displayed are both (a) inlet and (b) outlet headers. Air working fluid is represented by grey regions in the header structure, and is represented by red areas in the pipe flow relationship. Total irreversible pressure loss in the air headers is calculated to be less than 0.2%.
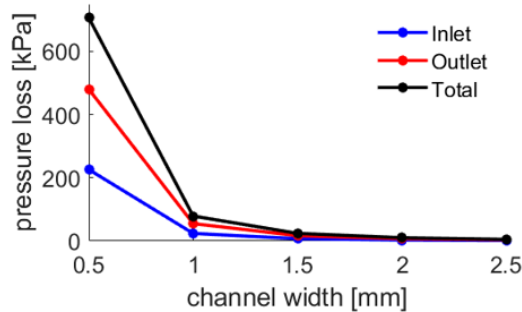
Figure 22 – Pressure loss with respect to channel width for inlet and outlet sCO_2 headers. A channel width of 1.5 mm achieves uniform mass distribution (Figure 18) and minimizes irreversible pressure losses, without significantly reducing header mechanical strength.

Using this approach, the pressure loss is estimated as 0.1% of the operating pressure (250 bar) in the sCO_2 headers and 0.2% of the operating pressure (80 bar) in the air headers. Overall this analysis highlights the insignificance of the pressure losses in headers relative to the target pressure drop of 4% for the total system. The dominant pressure drop occurs due to viscous losses through the HX core [23].

4.2.2. Thermal, structural performance

Due to the large temperature difference between heat transfer fluids, the sCO_2 header machined directly into the heat exchanger core experiences large temperature gradients. To verify that thermal strains will not impact structural integrity, a 3D COMSOL model shown in Figure 23 was developed using the thermal expansion multiphysics coupling in version 5.5. Roller constraints were placed on the top and bottom of the header, free to move in-plane, while symmetry conditions were applied to the left and right sides. The simulation results indicate a possible displacement of up to 12 μm due to thermal gradient-induced deformation, reducing the channel width by 0.8%. This will have a negligible impact on performance, as shown in Figure 18 and Figure 22. In addition, this model showed that 1st principal stress concentrated at sharp corners on the order of 100 MPa, due to the pressure and thermal loading. With the locations of concern identified, round endmills can be used during machining to fillet these corners and drastically reduce the tensile stress concentrations.
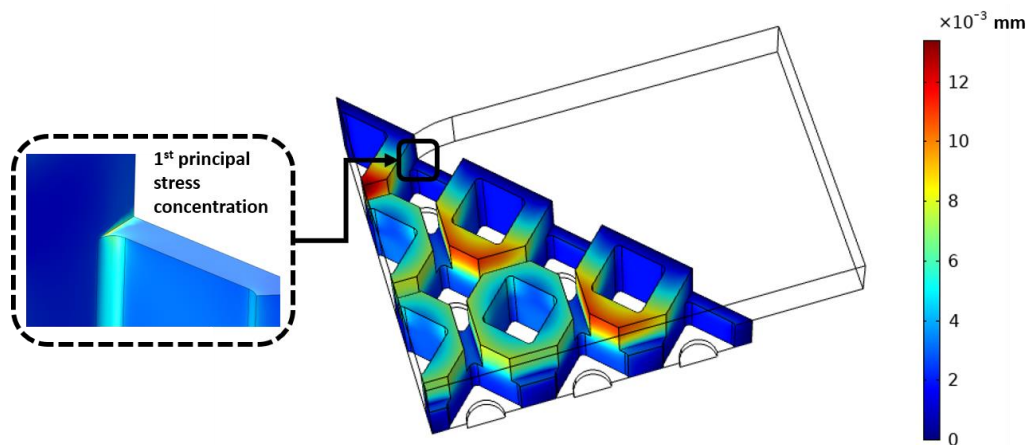
Figure 23 – 3D COMSOL simulation of sCO_2 header with both pressure loads and thermal gradients applied. The resulting displacement shown is a maximum of 12 μm, or 0.8% of the channel width.

Finally, a 2D structural simulation of the milled sCO_2 header was done with the microscale detailed structures to analyze the impact material removal had on structural integrity. Machining a channel into the heat exchanger core has no detrimental impact on microscale tensile stress concentrations, as shown in Figure 24. However, a channel larger than 1.5 mm opens the doorway for manufacturing defects to play a significant role, so overall the minimum channel width that allows for adequate header performance is recommended to be 1.5 mm.
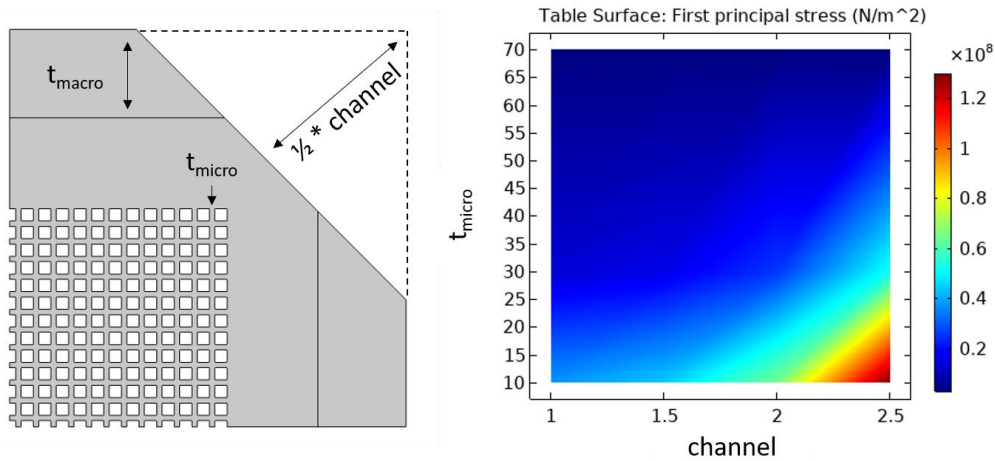
Figure 24 – 2D COMSOL simulation of ¼ of an air macrochannel with a corner removed to account for the milling of channels necessary for the sCO₂ header. Maximum 1ˢᵗ principal stress values of ~ 20 MPa occur at the upper right microchannel corner, yielding a safety factor of 10.

4.2.3. Next steps for header evaluation

While the current header design theoretically achieves our targets for 4% pressure loss and adequate flow distribution, experimental data is required to validate both conclusions and build confidence in our design. Future work will experimentally test prototype headers produced by our collaborators at Purdue University, using the experimental setup in Chapter 5. Additionally, the mechanical strength of interfaces formed during joining of the header components will need to be quantified, as these are potential weak points in the heat exchanger. The parametric sweep data shown here will allow us to rapidly evaluate design iterations if the need arises due to unforeseen manufacturing difficulties, as the next steps overall in header evaluation will focus on realizing this design.

Chapter 5

5. Experimental setup

5.1. DETERMINATION OF CUSTOM MATERIAL PROPERTIES

Our research collaborators at Purdue University are developing a custom SiC blend to meet the project requirements for a high-temperature, strong ceramic that can be repeatedly co-extruded to achieve the proposed design. So far, we have evaluated several potential material candidates based on their thermal conductivities and present the results below. Future work involves mechanically testing the materials and finalizing a material blend, both of which will be done in conjunction with the Purdue team.

5.1.1. Thermal conductivity measurements

Thermal conductivity values of various custom SiC samples were determined using a three-step process. First, the laser flash method [54] was employed using a Netzsch LFA 457 MicroFlash® to determine a material's thermal diffusivity using equation (14). Next, a differential scanning calorimeter (Netzsch 404 Pegasus® high-temperature DSC) was used to determine the specific heat of each sample. Finally, both data sets were combined via equation (15) to determine the thermal conductivity of each SiC sample. Both equations are as follows,

$$a = 0.1388 \frac{l^2}{t_{0.5}} \tag{14}$$

$$k = a\rho C_p \tag{15}$$

where a is the thermal diffusivity of the material, ρ is the density of the material, C_p is the specific heat, l is the thickness of the sample, and t is the time for the sample temperature to increase 50% of targeted temperature. The results of these measurements are summarized in Figure 25.
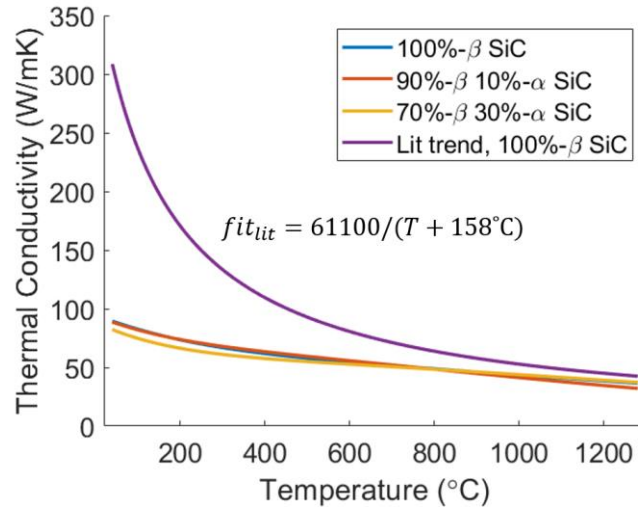
Figure 25 – Thermal conductivity of 3 SiC blends, compared to the literature value for monocrystalline β-SiC previously used in heat transfer modelling efforts [55]**. All samples of dense, polycrystalline SiC have similar thermal conductivities throughout the operating temperature range, regardless of α, β species concentrations. Thermal conductivity of the heat exchanger solid material ranges from 40-70 W/mK and is input as a temperature-dependent function to refine our models.**

Prior to experimenting with SiC samples from the Purdue team, heat transfer models of the heat exchanger used the literature trend in Figure 25 to define the thermal conductivity of SiC. However, there is a difference between our SiC blend values and literature values for monocrystalline SiC [55], due to the polycrystalline aspect of the sample material. This leads to a decrease in thermal conductivity because of thermal interfacial resistance between sintered particles. An effective medium approximation model [56][57] is used here to validate these thermal conductivity measurements by including the effect of interfacial resistance on thermal conductivity of a solid. For a solid with a defined particle size d, interfacial resistance is related to an effective conductivity by equation (16),

$$\frac{1}{k_{eff}} = \frac{1}{k_{solid}} + \frac{2R_i}{d} \qquad (16)$$

where k_{solid} is the thermal conductivity of the particle or a monocrystalline sample and R_i is the interfacial resistance between particles in a powder-sintered sample of SiC. Results of this analysis are shown in Figure 26, where interfacial resistances are calculated from the thermal conductivity data assuming an expected grain size of 1-5 μm [38].
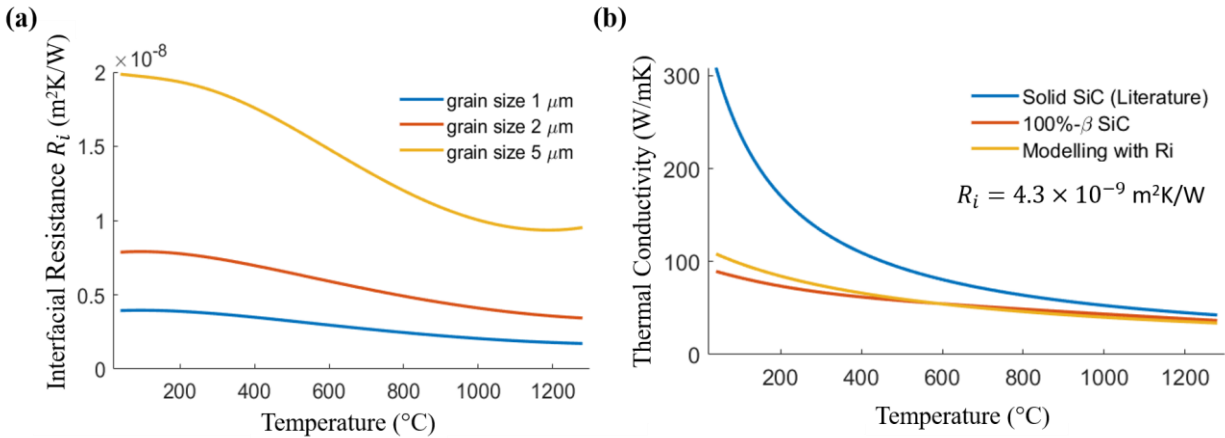
Figure 26 – Analysis of interfacial resistance. R_i values extracted from experimental data at each temperature. (a) Relatively constant and small values of R_i indicate good sintering, and (b) good agreement between interfacial resistance model and 100%-β SiC samples validates the assumption of interfacial resistance dominance and negligible effect of porosity.

Interfacial resistance values extracted from experimental data are small and relatively constant across the sample temperature range, which indicates good sintering in the SiC samples. Also, experimental values match the interfacial resistance model for a grain size of 1.5 μm, a grain size which is consistent with preliminary images of the 100%-β SiC microstructure taken by the Purdue team. This agreement validates the hypothesis of interfacial resistance driving the difference between monocrystalline literature values and experimental values of thermal conductivity. Additionally, experimental values for thermal conductivity closely match those found by other researchers working with dense polycrystalline SiC [58], further supporting the claim that the thermal conductivity values presented here are accurate and thus will be used in the future to refine thermal models of the heat exchanger core.

5.1.2. Material decision and potential model impacts

100%-β SiC will be used moving forward due to the preference of the manufacturing team and an indifference of thermal conductivity to sample type. Consequently, this material choice has a negligible impact on the overall thermal performance of the heat exchanger. In the future α, β SiC structure concentrations can be varied to achieve a target material strength or hardness without concern for the thermal performance of the system.

5.2. EXPERIMENTAL SETUP FOR HEAT EXCHANGER PROTOTYPES

A custom leak-proof compressed air setup was designed and fabricated to test various components of the heat exchanger during development at MIT. Although the setup is not designed to achieve target operating temperatures and pressures, it will allow for initial performance characterization of the fabricated HX. Temperature and pressure data are independently obtained both before and after the heat exchanger for each flow loop, which will be used to determine heat exchanger effectiveness and power density. Furthermore, pressure loss and heat transfer will be quantified. With this less-extreme testing we aim to validate and refine our models, as well as address any unforeseen difficulties prior to high-temperature, high-pressure experimentation. Figure 27 shows the paths of the working fluids, while Figure 28 displays the finished setup. Insulation is present in the final setup but removed for illustration purposes only.
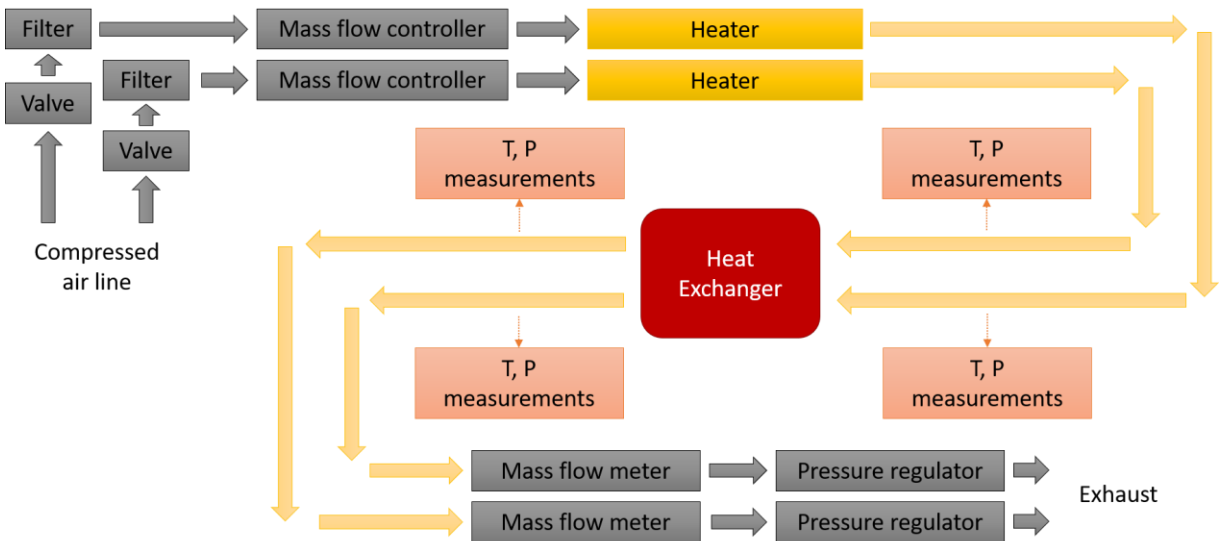
Figure 27 – Test setup schematic. The architecture consists of two independent compressed air lines, each following a similar path through the open-loop system. First valves are in place to start and stop the air, followed by a 0.5 µm air filter and mass flow controller. Then, temperature and pressure measurements (T, P) are taken both before and after the component being tested, followed by a mass flow controller and a back-pressure regulator per air path.

All tubing components, unless otherwise specified in this section, are 316L stainless steel and purchased from Swagelok [59]. Mass flow controllers (MCR-100SLPM-D, Alicat Scientific) and mass flow meters (M-100SLPM-D, Alicat Scientific) [60] are used to regulate the compressed air, with measuring capabilities $0.00 - 100.00 \pm 0.01$ SLPM. TUTCO SureHeat threaded inline air heaters are used to change the temperature of the air working fluid [61], with the maximum temperature constrained by the steel tubing to 537 °C. Heaters and their corresponding thermocouple adaptors are cemented together using X-Pando high-

temperature thread sealant for a leak-proof seal. K-type thermocouple probes (KQXL-18G-12, Omega Engineering) are installed in the air stream to measure gas temperature, and stainless-steel strain gauge pressure transducers (PX309-100GI, Omega Engineering) are used to measure static pressure. These measurements are recorded using a compactDAQ chassis (cDAQ-9174, National Instruments) with an 8-channel thermocouple adaptor (NI 9212, National Instruments) and a 32-channel voltage adaptor (Ni 9205, National Instruments). Back pressure for the whole system is regulated using two back pressure regulators (KBP1F0D4A5A20000, Swagelok). The safety housing is made of ¼" acrylic sheets, laser-cut to fit on an aluminum extrusion frame, with an impact strength of 20 J/m. Vents at the top allow for air to circulate, as well as cables to move in and out of the enclosure.
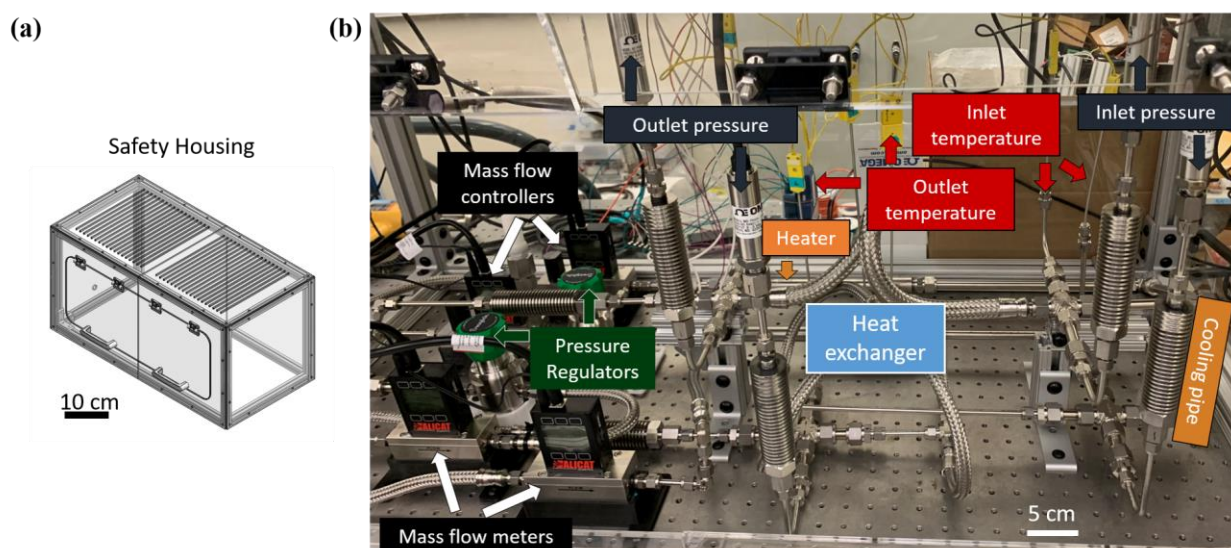
Figure 28 – Self-contained in an acrylic safety housing (a) and fabricated test setup (b).

5.2.1. Fabrication challenges, leak testing

Flexible stainless-steel tubing was essential to this setup as it allowed for increased tolerance between tubes and components. Corners and bends were more easily achieved with flexible tubing, rather than standard 316L SS tubing and connectors. Tubes were connected with Swagelok tube fittings when possible, as these connections are rated for vacuum seals and are easy to install, disassemble, and replace. All other connections were national pipe tapered (NPT) threads. Cycle components, such as mass flow controllers and pressure regulators, are mounted to the worktable using custom part holders that restrict motion during tube adjustment and/or replacement. Both cycles are leak-tested using a helium leak detector according to the procedures from literature [62]. Initially, it was found that many threaded pipe fittings (NPT, ½" - 20 and ¼" - 20) were not sealed properly and leaked during operation. Sealant selections were limited due to

the target 400 °C operating temperature. Several sealants were tested to alleviate this issue, with X-Pando high-temperature thread sealant achieving the best seal with a leak rate of 4.6×10^{-10} $mbar*l*s^{-1}$. The entire cycle is insulated using fiberglass insulation, and the flow is cooled using cooling elements prior to pressure transducers and mass flow meters. Insulation and cooling capabilities are currently being refined by adjusting the insulation thickness and number of cooling elements, such that minimal heat is unintentionally lost to the environment at 400 °C and the pressure transducers experience temperatures below 60 °C. Achieving optimal temperatures remains an ongoing challenge in the use of this experimental setup at high temperatures.

5.3. PRESSURE DROP MEASUREMENT

Thus far the experimental setup has been used to test four proof-of-concept macrochannels, one of which is shown in Figure 29. Current fabrication tooling limits the geometric parameters in these samples vary from the ideal case presented previously in this thesis (225 instead of 625 microchannels arranged in a 3×3 mm array rather than a 5×5 mm array with targeted microchannel sizes of 120 μm instead of 140 μm). Nonetheless, the samples do provide validation that co-extruded microchannels are feasible. The goal of testing these samples is to experimentally relate pressure drop measurements to the average hydraulic diameter and tortuosity of a microchannel, while demonstrating the functionality of the test setup. Overall, this evaluates our current performance capabilities and provides validation for the setup, as well as a first look into how precise the manufacturing method is providing with the current tooling. Future plans for experimentally testing the heat exchanger core and headers are discussed in the next section.
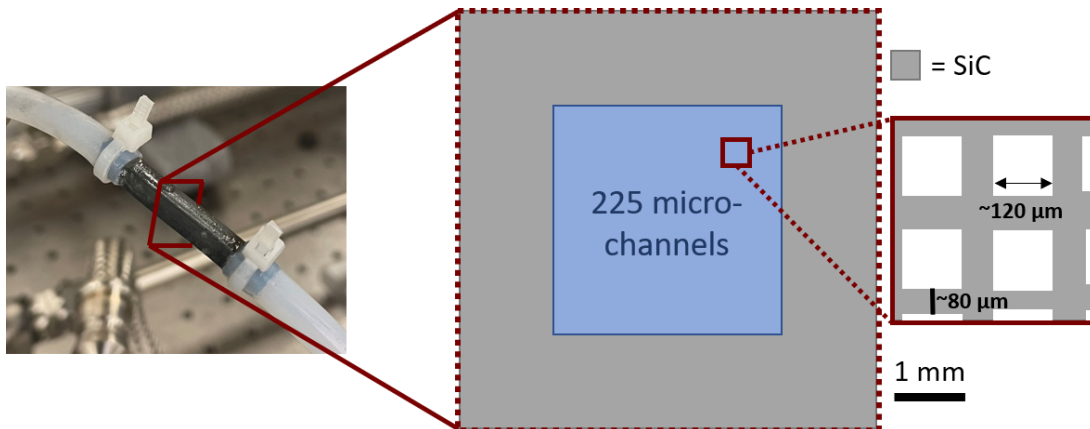

Figure 29 – Experimental macrochannel, consisting of 225 microchannels each with a square opening theoretically 120 μm in size and walls 80 μm. The entire 225 microchannel cluster is cladded in a solid SiC wall 1 mm thick.

Pressure drop data was gathered using the experimental setup introduced previously. Volumetric flow rate was varied from 1-7 SLPM, with a working fluid of air at 25 °C and an outlet condition of 1 bar (atmospheric pressure) for the system. No significant (> 0.01 SLPM) leaks were measured across the flow domain for any sample. Pressure drop and flow rate data, converted to microchannel volumetric flow rate using equation (17), were then fed to equation (18) to calculate the average hydraulic diameter D_h of a microchannel. Hydraulic diameters of all four samples are shown in Table 5. Equation (18) is the Darcy-Weisbach equation [53], an empirical formula for relating the pressure loss due to friction along a length of pipe to the average velocity and cross-sectional area in the case of an incompressible fluid.

$$v = x \, [SLPM] * \frac{T_g}{298.15[K]} * \frac{1.01325 \, [bar]}{P_g} * \frac{1[L]}{1000[m^3]} * \frac{1}{nchannels} * \frac{1 \, min}{60 \, s} \tag{17}$$

$$\frac{\Delta P}{L} = \frac{32\mu v}{D_h^4} \tag{18}$$

Lengths L of all samples were measured using a digital caliper, and viscosity μ of the working fluid was taken from literature [48] for air at room temperature: $\mu = 1.81 * 10^{-5} \left[\frac{kg}{ms}\right]$. Propagation of error [63] was preformed to determine the precision of hydraulic diameter estimations given uncertainties in experimental processes using equation (19). These experimental uncertainties are due to measurement equipment limitations, and are as follows: flow rate $v \pm 0.01$ SLPM, length $L \pm 0.1$ mm, pressure drop $\Delta P \pm 200$ Pa.

$$\frac{\sigma_{D_h}}{D_h} = \frac{1}{4}\sqrt{\left(\frac{\sigma_v}{v}\right)^2 + \left(\frac{32 * \sigma_\mu}{32 * \mu}\right)^2 + \left(\frac{\sigma_L}{L}\right)^2 + \left(\frac{\sigma_{\Delta P}}{\Delta P}\right)^2} \tag{19}$$

Table 5 – Average hydraulic diameter of the microchannels internal to each sample, determined using equation (18), measured pressure drop, and length of sample.

Sample #	Hydraulic Diameter D_h [μm]
1	89.8 ± 0.1
2	89.6 ± 0.2
3	83.7 ± 0.1
4	94.9 ± 0.2

To validate Table 5 data, cross-sectional images were taken and microchannel sizes were directly measured using image processing techniques in MATLAB R2019b.
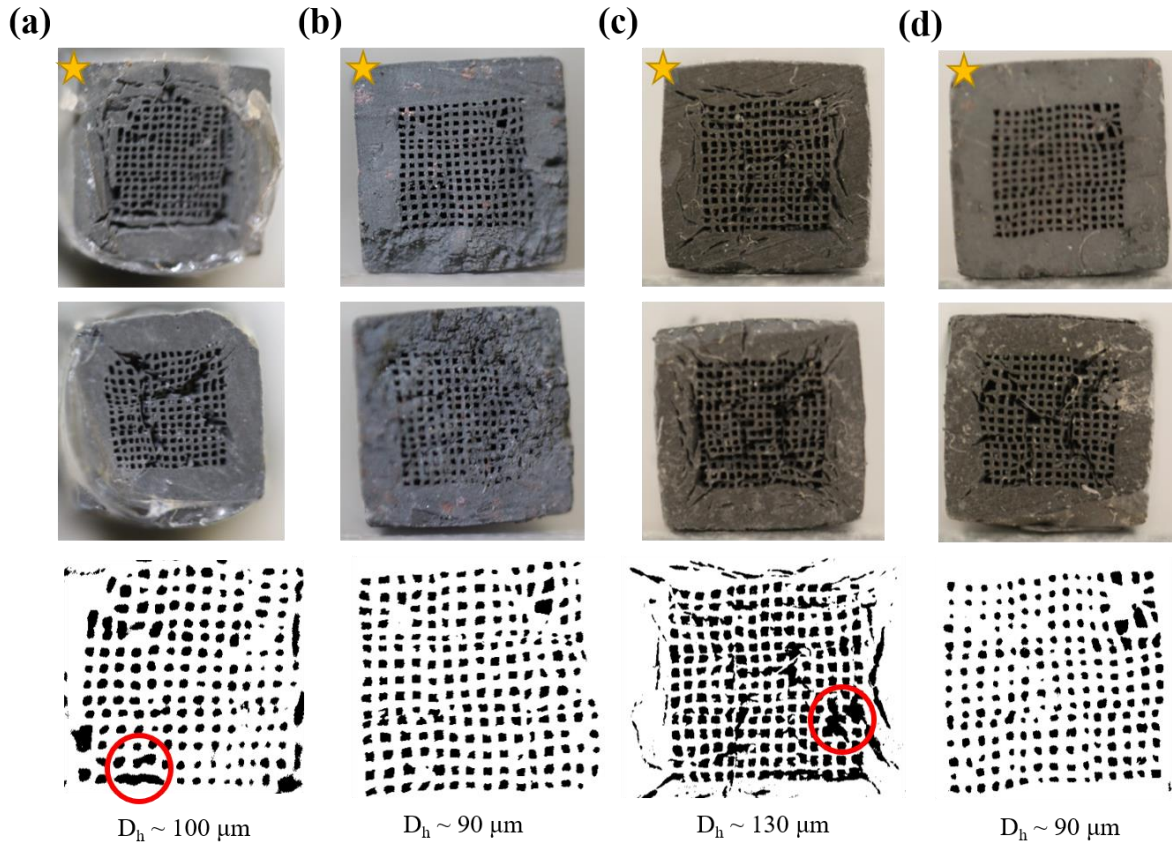
Figure 30 – Images of sample unit cells from the team at Purdue University, numbered 1-4 from (a) to (d). Starred images are repeated in black and white for hydraulic diameter measurements. Surface defects, examples of which are highlighted in red, limited the accuracy of samples 1 (a) and 3 (c). All data is reported to the nearest 10 μm. Samples 2 and 4, whose surfaces were more well-defined, have average microchannel sizes of 90 μm, in good agreement with the predicted data in Table 5.

Large defects on the surface of the samples limit the precision of the imaging approach, as shown in Figure 30; however, rough measurements do agree well with hydraulic diameters predicted in Table 5 and therefore support the conclusion of relatively non-tortuous microchannels. Overall, good agreement between visual measurements and predictions using the Darcy-Weisbach relationship of D_h validates the pressure drop measurements and demonstrates straight microchannels in the samples. Although these conclusions are promising, further manufacturing optimization is required to identify the cause of microchannel size mismatch and to achieve the target hydraulic diameter of 140 μm in a low-defect sample. Figure 31 summarizes the measurements for each sample, as well as extrapolates the average to predict pressure drop values if the samples were used at the target operating conditions for the air working fluid (8 MPa, 1285 °C). For a heat exchanger core length of 40 mm, these sample architectures would create an irreversible

pressure drop on the order of 0.8 MPa, or 10% total pressure loss. To achieve the target 4% pressure drop with these samples, under the sample flow conditions and overall dimensions, the Darcy-Weisbach relationship plotted in Figure 32 states microchannels larger than 117 μm are necessary.
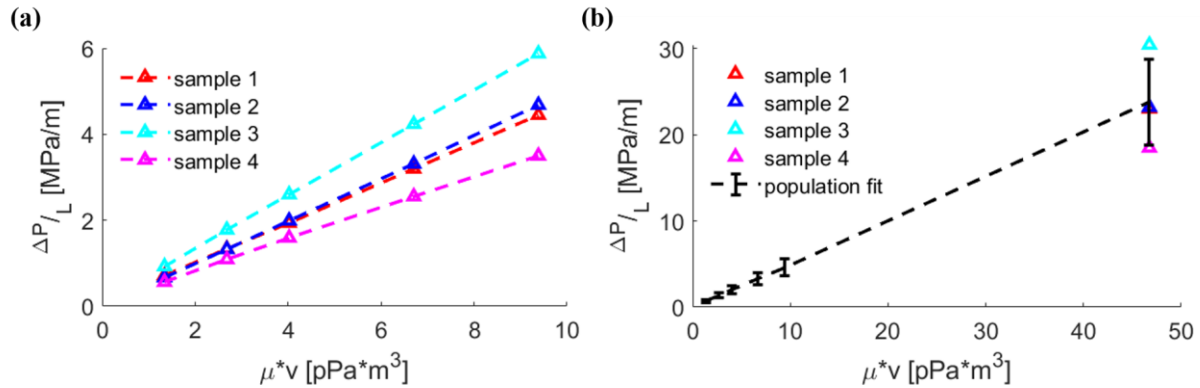
Figure 31 – (a) Sample data for four unit cells normalized by sample length. (b) Pressure drop data extrapolated to high-temperature, high-pressure operating conditions (air – 80 bar, 1285 °C) using Darcy-Weisbach relationship. Good agreement is achieved between experimental data and pressure drop prediction using hydraulic diameters determined by Darcy-Weisbach.
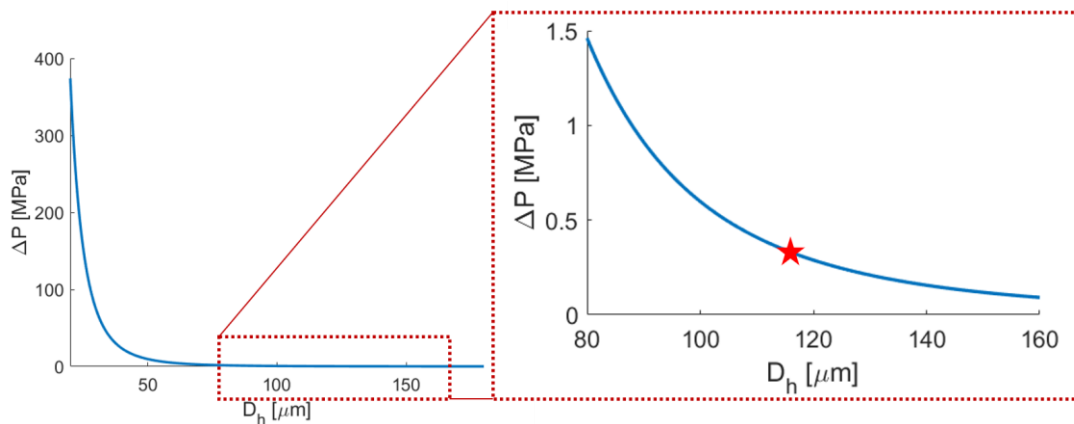
Figure 32 – Pressure drop ΔP as a function of hydraulic diameter D_h, based on operating viscosity and velocity of air at 1285 °C, 8 MPa, with a length of 40 mm. To maintain a pressure drop throughout the core < 4%, these 225 microchannel unit cells would need a $D_h > 117$ μm as marked by a red star.

In conclusion, despite mismatch between expected microchannel size with the experimental data, the co-extrusion process has managed to produce open and thorough microchannels for the multiscale heat exchanger. With revised design and optimized fabrication process, the initial characterization of the unit

cells has shown great promises to demonstrate high power density, robust mechanical strength, and low pressure drop within a scalable and low-cost manufacture method.

5.4. FUTURE CHARACTERIZATION PLAN

As the project progresses from a manufacturing standpoint this experimental setup will be used to rapidly characterize hydraulic diameters of various microchannel extrusions, as well as evaluate irreversible pressure losses in header designs and total heat exchanger prototypes at both ambient conditions and higher-temperature, higher-pressure conditions. Moreover, this setup will be used to test prototype cycle connections currently being designed for both the MIT test setup and General Electric's high temperature experimental testing facilities. These cycle connections pose a significant challenge to heat exchanger operation, depending both on material behavior and manufacturing capabilities, and as such are a priority moving forward.

Chapter 6

6. Future work and challenges

In this thesis we presented the modelling and design of a multiscale heat exchanger for use in high-temperature, high-pressure thermodynamic cycles, specifically a sCO_2 Brayton cycle. The proposed heat exchanger core design, featuring a SiC microstructure fabricated using ceramic co-extrusion techniques, was geometrically optimized to maintain a theoretical safety factor of 2.5 against mechanical failure while achieving designated thermal performance metrics. Multi-physics models of a header design to interface the core with cycle tubing were also presented, featuring geometries that were optimized to achieve minimal flow maldistribution (6 g/s) and pressure loss (< 0.2 %). Finally, an experimental setup was developed to evaluate the performance of the heat exchanger core and header prototypes. Setup capabilities were demonstrated by evaluating the pressure loss of several heat exchanger core macrochannels, with experimental results providing a baseline for current project capabilities.

6.1. FABRICATION

While the fabrication of the heat exchanger by our collaborators at Purdue University is ongoing, it is our goal to propose a design here that provides sufficient flexibility to account for synthesis limitations. Section 3.6 introduces a potential HX core design variation to account for materials with tensile limits lower than that seen in literature, while the experimental setup framework in section 5.2 can be used to rapidly test any heat exchanger subcomponents, either to validate numerical models or quantify manufacturing variations. One component with a high likelihood of variation for specific applications is the heat exchanger headers due to its reliance on co-sintering and/or bonding of multiple SiC parts, which is historically a difficult process. Future work will be done in collaboration with our partners at Purdue University, using the model frameworks presented here, to account for any unforeseen manufacturing constraints.

6.2. LIFETIME CONCERNS, FATIGUE OF SILICON CARBIDE

Due to the cyclical nature of loading and unloading a heat exchanger, concerns about fatigue and sub-critical crack growth need to be addressed. Pending successful fabrication of heat exchanger prototypes, the experimental setup shown in chapter 5 will be used to cyclically stress-test our design and potentially address these lifetime concerns.

6.3. FUTURE WORK

This thesis is written half-way through the project timeline, and as such changes are inevitable. Future work will continue to develop the designs presented here and devise alterations to increase its manufacturability and survivability for various cycle applications, as the design benefits presented here are not limited to sCO_2 Brayton cycle architectures. Mating of the heat exchanger to cycle architecture is a major design hurtle that will be a priority in the near future, as well as continuing model refinement based on experimentally obtained material properties.

7. Bibliography

[1]   EIA, "Electric Power Annual," *Eia.Doe.Gov*, vol. 0348, no. January, p. 2, 2010.

[2]   U. S. E. I. Administration, *January 2021 Monthly Energy Review*, vol. 0035, no. January. 2021.

[3]   M. Höök and X. Tang, "Depletion of fossil fuels and anthropogenic climate change-A review," *Energy Policy*, vol. 52, pp. 797–809, 2013.

[4]   M. T. Dunham and B. D. Iverson, "High-efficiency thermodynamic power cycles for concentrated solar power systems," *Renew. Sustain. Energy Rev.*, vol. 30, pp. 758–770, 2014.

[5]   D. Scholz, "An Optiomal APU for Passenger Aircraft," 2015.

[6]   K. Brun, P. Friedman, and R. Dennis, *Fundamentals and applications of supercritical carbon dioxide (sCO2) based power cycles*. Woodhead publishing, 2017.

[7]   S. R. Penfield, "Compact Heat Exchangers for Nuclear Power Plants," *Top. Work. New Cross-Cutting Technol. Nucl. Power Plants*, 2017.

[8]   J. Serp *et al.*, "The molten salt reactor (MSR) in generation IV: Overview and perspectives," *Prog. Nucl. Energy*, vol. 77, pp. 308–319, 2014.

[9]   S. a Wright, R. F. Radel, M. E. Vernon, G. E. Rochau, and P. S. Pickard, "Operation and Analysis of a Supercritical CO2 Brayton Cycle," *SANDIA Rep. SAND2010-0171*, no. September, p. 101, 2010.

[10]   P. M. Sforza, *Commercial airplane design principles*. Elsevier, 2014.

[11]   A. I. K. Aviation, "Fuel Consumption of Popular Aircraft," 2019. [Online]. Available: https://alliknowaviation.com/2019/12/14/fuel-consumption-aircraft/.

[12]   V. Dostal, P. Hejzlar, and M. J. Driscoll, "The supercritical carbon dioxide power cycle: Comparison to other advanced power cycles," *Nucl. Technol.*, vol. 154, no. 3, pp. 283–301, 2006.

[13]   X. Zhang *et al.*, "Recent developments in high temperature heat exchangers: A review," *Front. Heat Mass Transf.*, vol. 11, 2018.

[14]   R. K. Shah and D. P. Sekulić, "Chapter 17. Heat Exchangers," *J. Fuel Cell Sci. Technol.*, 1998.

[15]   Q. Li, G. Flamant, X. Yuan, P. Neveu, and L. Luo, "Compact heat exchangers: A review and future

applications for a new generation of high temperature solar receivers," *Renew. Sustain. Energy Rev.*, vol. 15, no. 9, pp. 4855–4875, 2011.

[16]   M. Caccia *et al.*, "Ceramic–metal composites for heat exchangers in concentrated solar power plants," *Nature*, vol. 562, no. 7727, pp. 406–409, 2018.

[17]   A. H. Rashed, "Properties and Characteristics of Silicon Carbide," 2002.

[18]   Morgan Advanced Ceramics, "Data Sheet Performance CVD SiC," no. 286773, p. 286773, 2013.

[19]   "Inconel Alloy 625 Data Sheet."

[20]   High   Temp   Metals,   "Rene   41   Technical   Data."   [Online].   Available: https://www.hightempmetals.com/techdata/hitempRene41data.php. [Accessed: 03-Feb-2021].

[21]   R. K. Shah, *Fundamentals of heat exchanger design*. John Wiley & Sons, Inc., 2003.

[22]   M. Kaviany, *Principles of Heat Transfer in Porous Media*. 2006.

[23]   E. Wang *et al.*, "Devices and Methods for Fabrication of Components of a Multiscale Porous High-Temperature Heat Exchanger," 63/166973, 2021.

[24]   Y. Ahn *et al.*, "Review of supercritical CO2 power cycle technology and current status of research and development," *Nucl. Eng. Technol.*, vol. 47, no. 6, pp. 647–661, 2015.

[25]   ARPA-E, "HITEMMP Project Descriptions," pp. 1–4, 2019.

[26]   A. T. Crumm and J. W. Halloran, "Fabrication of microconfigured multicomponent ceramics," *J. Am. Ceram. Soc.*, vol. 81, no. 4, pp. 1053–1057, 1998.

[27]   T. Ohji, *Testing and Evaluation of Mechanical Properties*, Second Edi. Elsevier, 2013.

[28]   J. F. Shackelford, Y.-H. Han, S. Kim, and S.-H. Kwon, *CRC Materials Science and Engineering Handbook*. 2016.

[29]   F. P. Beer, J. E. Russell Johnston, J. T. DeWolf, and D. F. Mazurek, *Mechanics of Materials*, Sixth Edit. McGraw-Hill, 2012.

[30]   D. Roylance, "Introduction to Fracture Mechanics," 2001.

[31]   F. Beer, E. Johnston, J. DeWolf, and D. Mazurek, *Mechanics of Materials, 5th Edition*, 5th Editio. McGraw-Hill, 1999.

[32]   H. Sonnerlind, "Singularities in Finite Element Models: Dealing with Red Spots," 2015. [Online].

Available: https://www.comsol.com/blogs/singularities-in-finite-element-models-dealing-with-red-spots/. [Accessed: 03-Jan-2020].

[33] W. Pabst, E. Gregorová, and G. Tichá, "Elasticity of porous ceramics - A critical study of modulus-porosity relations," *J. Eur. Ceram. Soc.*, vol. 26, no. 7, pp. 1085–1097, 2006.

[34] U. Imke, "Porous media simplified simulation of single- and two-phase flow heat transfer in micro-channel heat exchangers," *Chem. Eng. J.*, vol. 101, no. 1–3, pp. 295–302, 2004.

[35] D. M. Liu, Z. C. Jou, B. W. Lin, and C. T. Fu, "Microstructure and high-temperature strength of pressureless-sintered silicon carbide," *J. Mater. Sci. Lett.*, vol. 14, no. 19, pp. 1327–1328, 1995.

[36] A. A. Griffith, "The Phenomena of Rupture and Flow in Solids," *R. Publ. Soc.*, vol. CCXXI, 1920.

[37] G. R. Irwin, "Analysis of Stresses and Strains near the End of a Crack Traversing a Plate," *J. Appl. Mech.*, vol. 24, pp. 361–364, 1957.

[38] Y.-W. Kim, M. Mitomo, and H. Hirotsuru, "Grain Growth and Fracture Toughness of Fine-Grained Silicon Carbide Ceramics," *J. Am. Ceram. Soc.*, vol. 78, no. 11, pp. 3145–3148, 1995.

[39] D. M. Liu and C. T. Fu, "Effect of residual porosity and pore structure on the mechanical strength of SiC-Al2O3-Y2O3," *Ceram. Int.*, vol. 22, no. 3, pp. 229–232, 1996.

[40] R. A. Alliegro, J. R. Tinklepaugh, and L. Coffin, "Pressure-Sintered Silicon Carbide," *J. Am. Ceram. Soc.*, vol. 39, no. 11, pp. 386–389, 1956.

[41] T. Y. Cho, Y. W. Kim, and K. J. Kim, "Thermal, electrical, and mechanical properties of pressureless sintered silicon carbide ceramics with yttria-scandia-aluminum nitride," *J. Eur. Ceram. Soc.*, vol. 36, no. 11, pp. 2659–2665, 2016.

[42] J. F. Plourde, T. Mosidis, and B. J. Fichera, "Heat Exchanger With Headering System and Method for Manufacturing Same," 13/442,531, 2013.

[43] D. K. Harris, D. G. Warren, and V. W. Goldschmidt, "Impact of manifold design on heat exchanger efficiency," *J. Heat Transfer*, vol. 119, no. 2, pp. 357–362, 1997.

[44] V. L. Wiesner, J. P. Youngblood, and R. W. Trice, "Room-temperature injection molding of aqueous alumina-polyvinylpyrrolidone suspensions," *J. Eur. Ceram. Soc.*, vol. 34, no. 2, pp. 453–463, 2014.

[45] X. Peng, D. Li, J. Li, S. Jiang, and Q. Gao, "Improvement of flow distribution by new inlet header configuration with splitter plates for plate-fin heat exchanger," *Energies*, vol. 16, no. 3, 2020.

[46]   K. D. Timmerhaus, *Advances in Cryogenic Engineering*. Springer Science and Business Media, LLC, 1966.

[47]   A. Raul, B. N. Bhasme, and R. S. Maurya, "A numerical investigation of fluid flow maldistribution in inlet header configuration of plate fin heat exchanger," *Energy Procedia*, vol. 90, no. December 2015, pp. 267–275, 2016.

[48]   D. R. D. Pijush K. Kundu, Ira M. Cohen, *Fluid Mechanics*. .

[49]   D. C. Wilcox, *Turbulence Modelling for CFD 3rd Edftion*. 2006.

[50]   Neutrium, "Pressure Loss from Fittings - Expansion and Reduction in Pipe Size," 2012. [Online]. Available: https://neutrium.net/fluid-flow/pressure-loss-from-fittings-expansion-and-reduction-in-pipe-size/.

[51]   P. Ellenberger, *Piping and Pipeline Calculations Manual*. Elsevier Inc., 2010.

[52]   K. T. Trinh, "On the Blasius correlation for friction factors," no. 1932, 2010.

[53]   F. M. White, *Fluid Mechanics*, Sixth Edit. McGraw-Hill, 2008.

[54]   W. J. Parker, "Flash Method of Determining Thermal Diffusivity, Heat Capacity, and Thermal Conductivity," *J. Appl. Phys.*, vol. 32, no. June, p. 1679, 1961.

[55]   O. Nilsson, "Determination of the thermal diffusivity and conductivity of monocrystalline silicon carbide (300-2300 K)," *High Temp. - High Press.*, vol. 29, pp. 73–79, 1997.

[56]   C. W. Nan, R. Birringer, D. R. Clarke, and H. Gleiter, "Effective thermal conductivity of particulate composites with interfacial thermal resistance," *J. Appl. Phys.*, vol. 81, no. 10, pp. 6692–6699, 1997.

[57]   X. Li, W. Park, Y. P. Chen, and X. Ruan, "Effect of particle size and aggregation on thermal conductivity of metal-polymer nanocomposite," *J. Heat Transfer*, vol. 139, no. 2, pp. 1–5, 2017.

[58]   D.-M. Liu and B.-W. Lin, "Thermal Conductivity in Hot-Pressed Silicon Carbide," *Ceram. Int.*, vol. 22, no. 1, pp. 407–414, 1996.

[59]   Swagelok, "Product Catalog."

[60]   A. Scientific, "Operating Manual."

[61]   T. SureHeat, "Threaded Inline Heaters," 2021.

[62]   H. Rottländer, W. Umrath, and G. Voss, "Fundamentals of leak detection," *Leybold*, no. 199, 2016.

[63]   H. Schenck, *Theories of Engineering Experimentation*, Third Edit. McGraw-Hill, 1979.